The Astrophysical Journal, 901:168 (21pp), 2020 October 1 https://doi.org/10.3847/1538-4357/abb1a0

Completing the Census of AGN in GOODS-S/HUDF: New Ultradeep Radio Imaging and Predictions for JWST

Stacey Alberts[1], Wiphu Rujopakarn[2,3,4], George H. Rieke[1], Preshanth Jagannathan[5], and Kristina Nyland[6]
[1] Steward Observatory, University of Arizona, 933 N. Cherry Ave., Tucson, AZ 85721, USA; salberts@email.arizona.edu
[2] Department of Physics, Faculty of Science, Chulalongkorn University, 254 Phayathai Road, Pathumwan, Bangkok 10330, Thailand
[3] National Astronomical Research Institute of Thailand (Public Organization), Don Kaeo, Mae Rim, Chiang Mai 50180, Thailand
[4] Kavli IPMU (WPI), UTIAS, The University of Tokyo, Kashiwa, Chiba 277-8583, Japan
[5] National Radio Astronomy Observatory, Socorro, NM 87801, USA
[6] National Research Council, resident at the Naval Research Laboratory, Washington, DC 20375, USA
Received 2020 May 6; revised 2020 August 20; accepted 2020 August 22; published 2020 October 6

Abstract

A global understanding of active galactic nuclei (AGN) and their host galaxies hinges on completing a census of AGN activity without selection biases down to the low-luminosity regime. Toward that goal, we identify AGN within faint radio populations at cosmic noon selected from new ultradeep, high-resolution imaging from the Karl G. Jansky Very Large Array at 6 and 3 GHz. These radio data are spatially coincident with the ultradeep legacy surveys in the GOODS-S/HUDF region, particularly the unparalleled Chandra 7 Ms X-ray imaging. Combined, these data sets provide a unique basis for a thorough census of AGN, allowing simultaneous identification via (1) high X-ray luminosity, (2) hard X-ray spectra, (3) excess X-ray relative to 6 GHz, (4) mid-IR colors, (5) SED fitting, (6) radio excess via the radio–infrared relation, (7) flat radio spectra via multiband radio, and (8) optical spectroscopy. We uncover AGN in fully half our faint radio sample, indicating a source density of one AGN arcmin^{-2}, with a similar number of radio-undetected AGN identified via X-ray over the same area. Our radio-detected AGN are majority radio-quiet, with radio emission consistent with being powered predominantly by star formation. Nevertheless, we find AGN radio signatures in our sample: ∼12% with radio excess indicating radio-loud activity, and ∼16% of radio-quiet AGN candidates with flat or inverted radio spectra. The latter is a lower limit, pending our upcoming deeper 3 GHz survey. Finally, despite these extensive data sets, this work is likely still missing heavily obscured AGN. We discuss in detail this elusive population and the prospects for completing our AGN census with James Webb Space Telescope/MIRI.

Unified Astronomy Thesaurus concepts: Active galactic nuclei (16); Radio galaxies (1343); Radio continuum emission (1340); High-redshift galaxies (734)

1. Introduction

Compelled by evidence such as the link between black hole (BH) mass and bulge properties in local galaxies (i.e., Magorrian et al. 1998), efforts to determine the extent of the coevolution between galaxies and BH growth via active galactic nuclei (AGN) remain at the forefront of galaxy evolution studies. This link appears to be fundamental, since it holds across multiple epochs, with the volume-averaged cosmic star formation (SF) and BH accretion histories both peaking at cosmic noon ($z \sim 1$–3), with a strong decline toward the present day (Madau & Dickinson 2014).

Definitive evidence for a causal connection has been elusive, however. For example, Diamond-Stanic & Rieke (2012) studied the Shapley-Ames Seyfert sample (low-luminosity, optically selected AGN) and found a correlation between the BH accretion rate (BHAR) and circumnuclear SF, but little such correlation for the total SF in the host galaxy. Chen et al. (2013) evaluated a more luminous mid-infrared (MIR) color and X-ray-selected sample, which showed a strong correlation between the BHAR and total host galaxy SF, a result that was confirmed by others (i.e., Delvecchio et al. 2015; Lanzuisi et al. 2017). On the other hand, Xu et al. (2015a) demonstrated, via an MIR-selected sample with spectroscopic follow-up, that an apparent correlation between SF and peak BHAR can arise from the dependence of each parameter on stellar mass—the SF through the main sequence, and the BHAR through the Magorrian relation—but without necessarily a more direct causal connection. This possibility had previously been suggested by Rafferty et al. (2011) and is supported by, e.g., Yang et al. (2017). Although both processes must be linked by a dependence on a common gas supply (i.e., Di Matteo et al. 2005; Smolčić et al. 2008; Hirschmann et al. 2014; Vito et al. 2014; Dai et al. 2018), these studies demonstrate that the details of their connection are not well understood observationally.

An attractive concept is that an evolutionary sequence links star-forming galaxies (SFGs) and rapidly accreting BHs (i.e., AGN), progressing from ultraluminous infrared galaxies (ULIRGs) to obscured AGN to unobscured AGN to quiescent galaxies (Hopkins et al. 2006). Direct and definitive evidence has been difficult to find, however, and the association of luminous AGN with main-sequence SFGs may even contradict the simplest form of this sequence (Xu et al. 2015a). Unfortunately, AGN–galaxy coevolution studies meant to quantify the SF/AGN relationship are fundamentally impeded by the difficulties in obtaining a complete census of AGN activity. It is now well established that all AGN selection techniques suffer from incompleteness and bias, typically driven by obscuration and viewing angle (i.e., Juneau et al. 2011; Caputi et al. 2014; Delvecchio et al. 2017).

To combat this issue, it is necessary to take advantage of the full (X-ray to radio) galaxy spectrum for AGN identification. Furthermore, survey depth strongly affects the outcome; deeper data, achieving better completeness at and below the boundaries between SF and AGN-dominated emission at a

given wavelength, generally reveal previously unknown AGN. In this work, we extend AGN identification by complementing the existing ultradeep legacy data sets in the GOODS-South/Hubble Ultra Deep Field (HUDF) region with new ultradeep radio data.

The radio spectrum provides a unique, yet complicated, tool in AGN identification and AGN–galaxy coevolution studies. At the bright end ($\gtrsim$1 mJy at $z \gtrsim 1$), low-frequency (<30 GHz) radio sources are universally understood to be dominated by bright, nonthermal synchrotron emission generated via AGN (i.e., Mignano et al. 2008). Typically, this synchrotron spectrum is optically thin and steep, associated with radiatively inefficient accretion activity (Meier 2002; Jester 2005; Fanidakis et al. 2011; Padovani 2016; Mancuso et al. 2017). However, radiatively efficient thin-disk accretion onto particularly massive BHs may produce a flat radio spectrum, such as in the case of blazars (Ghisellini et al. 2013; Padovani et al. 2017). Collectively, these bright radio sources are termed "radio-loud" (RL) or jetted, identified via radio morphological features and/or elevated radio emission relative to wavelength regimes that probe stellar emission (see Heckman & Best 2014; Kellermann et al. 2016; Padovani 2016, and references therein).

The radio picture is even more complex at the faint end. A flattening of the radio number counts below 1 mJy (e.g., Condon 1984; Windhorst et al. 1985; Hopkins et al. 1998; Richards 2000; Seymour et al. 2004; Simpson et al. 2006; Kellermann et al. 2008; Owen & Morrison 2008; Condon et al. 2012) points to distinct radio population(s), a mix of "radio-quiet" (RQ) AGN[7] and SFGs. In this regime, AGN are often by necessity identified at nonradio wavelengths and the mechanism(s) responsible for the bulk of the radio emission is unclear. There are multiple lines of evidence pointing to the radio spectra of most RQ AGN being dominated by SF, including radio-to-infrared ratios that are similar to those of SFGs (Bonzini et al. 2013, 2015; Padovani et al. 2015), as well as similarities in host galaxy colors, optical morphologies, and stellar masses between the SFG and RQ AGN populations (i.e., Kimball et al. 2011; Condon et al. 2013; Kellermann et al. 2016). On the other hand, studies of luminous RQ AGN (i.e., quasars) find elevated radio emission relative to expectations from current SF rates (SFRs; Zakamska et al. 2016; White et al. 2017), suggesting that a mix of SF and nuclear activity contributes to the radio outputs of these sources. High-resolution radio observations of RQ quasars and AGN find that the radio cores of such AGN contribute significantly to but do not dominate the total radio outputs (Jackson et al. 2015; Herrera Ruiz et al. 2016; Maini et al. 2016). Disentangling the sources of radio emission in the faint radio population is a necessary step toward utilizing the radio properly as an extinction-free SFR indicator and measure of AGN activity.

This paper explores AGN at the faint end of radio populations at cosmic noon ($z \sim$ 1–3), utilizing Very Large Array (VLA) imaging at 6 and 3 GHz at unprecedented depths (0.32 and 0.75 μJy beam^{-1}, respectively, at the pointing center). Combined with the ultradeep legacy data sets in GOODS-S/HUDF, we identify and characterize AGN within a radio-selected sample using multiple techniques: these include the radio–infrared relation, the presence of a flat slope between 3 and 6 GHz, and a high ratio of X-ray to 6 GHz luminosity. These methods are combined with purely X-ray identifications, the presence of MIR excesses, and optical spectroscopy, where available, to derive the most complete sample of AGN possible with the current data. We classify these AGN into RL and RQ and show that the radio emission of the RQ AGN in this faint sample is usually dominated by SF. Combining this radio-selected sample of AGN with X-ray AGN in radio-undetected galaxies over the same field allows us to put a lower limit on the number density of AGN. Finally, we broaden the discussion to what types of AGN may still be missing from our census and analyze the prospects for future detections with the James Webb Space Telescope (JWST), which will open up new avenues into identifying the most obscured AGN.

The paper is structured as follows: Section 2 presents the sample selection based on new VLA 6 GHz imaging, cross-matched with new 3 GHz imaging, existing ancillary data, and measured galaxy properties. Section 3 follows with a brief rundown of the demographics of our radio-selected sample. In Section 4, we identify AGN within our radio sample via multiple methods: X-ray-based selections, MIR excess via colors and spectral energy distribution (SED) fitting and decomposition, and radio signatures. We additionally identify AGN in radio-undetected galaxies over the relevant area using X-ray properties. A discussion of our results is provided in Section 5, including the nature of radio emission in galaxies containing AGN, the source density of AGN at cosmic noon, and prospects for identifying and characterizing the most heavily obscured AGN, a population still largely missing from current surveys. Section 6 contains our conclusions. Throughout this paper, we adopt the convention $S_\nu \propto \nu^\alpha$ for the radio spectral slope, where S_ν is the radio flux density and α is the spectral slope. We assume a Chabrier (2003) initial mass function and (Ω_M, Ω_Λ, h) = (0.27, 0.73, 0.71) (Spergel et al. 2003).

2. Data

2.1. Radio Observations

Our main data sets are radio imaging obtained at 6 GHz (5 cm) and 3 GHz (10 cm) from the Karl G. Jansky VLA. For the former, 177 hr of C-band imaging (4–8 GHz) centered on the HUDF (α, δ = 3:32:38.6, −27:46:59.89) was obtained from 2014 March to 2015 September in A, B, and C configurations. Data reduction was performed as described in Rujopakarn et al. (2016) using the `Common Astronomy Software Applications (CASA)` package (McMullin et al. 2007). The final map has a $0\farcs31 \times 0\farcs61$ synthesized beam and rms noise of 0.32 μJy beam^{-1} at the pointing center.

3 GHz imaging was obtained in a single pointing with the same pointing center as above. This pointing was observed for 90 hr in A, BnA, and B configurations during 2018 January–June using the *S*-band receiver covering 2–4 GHz. The observations comprised 36 dynamically scheduled sessions of 1.5–4 hr. Each session observed 3C 48 for flux and bandpass calibrations; J0402–3147 was observed for phase calibration every 25 minutes. The data reduction and extracted source catalog for the 3 GHz survey will be presented in W. Rujoparkarn (2020, in preparation); we summarize the data reduction here. Calibration and imaging were done with `CASA` using the following steps: (1) calibration and flagging of data

[7] Various other terms have been introduced to be more descriptive of possible mechanisms operating in these sources, e.g., "nonjetted" (Padovani 2016) or "core dominated" (Whittam et al. 2017).

using the VLA Data Reduction Pipeline (C. J. Chandler et al. 2020, in preparation), (2) removal of any portions of the data corrupted by strong radio frequency interference, and (3) imaging with the task TCLEAN. The imaging parameters were the following: MT-MFS deconvolver with nterms of 2 and Briggs weighting with robust parameter of 0.5, but with a pixel size of 0.″15. We imaged the 3 GHz data well beyond the primary beam radius of 7.′2 (employing the *w*-projection with wprojplanes of 128) to mitigate the imaging artifacts caused by the sidelobes from bright sources far from the pointing center. A wideband primary beam correction was applied to the 3 GHz (and 6 GHz) images using the CASA task WIDEBANDPBCOR. The final 3 GHz image has a $0.''6 \times 1.''2$ synthesized beam and rms noise at the pointing center of 0.75 μJy beam^{-1}.

For this work, source candidates were extracted from the 6 GHz map using the Python Blob Detection and Source Measurement (PyBDSM) software package (v1.8.6; Mohan & Rafferty 2015) down to 4σ on both the native resolution map and one with 300 $k\lambda$ tapering applied. The tapered map has a synthesized beam size of 0.″7 with a point-source sensitivity reduced by <6% compared to the native resolution map. Tapering is utilized to recover extended emission and mitigate the bias against less compact sources, generally SFGs (Guidetti et al. 2017). We expect the typical size of the radio-emitting region of an SFG at $z \sim 2$ to be ~0.″5 in diameter (Rujopakarn et al. 2016). Source fluxes are measured from the native or tapered map according to which maximizes the signal-to-noise ratio (S/N), defined as the ratio of the peak flux to the local rms. All 6 GHz sources were identified within the half-power radius ($r = 220''$) of the primary beam. Source extraction was performed on the 3 GHz image using the same technique at the native resolution. The 3 GHz catalog will be presented in W. Rujopakarn (2020, in preparation).

2.2. Optical–Far-infrared Counterparts and Final Radio Sample

6 GHz sources are confirmed via optical/near-infrared (NIR) counterparts, obtained by matching the 6 GHz catalog to the GOODS-S 3D-HST (v4.1) photometric catalog (Brammer et al. 2012; Skelton et al. 2014). This catalog provides coverage over 0.3–8 μm (observed) compiled from 20 photometric bands. To be considered in this study, we require each 6 GHz radio source to have an optical/NIR counterpart in 3D-HST and be at $z > 0.75$. We use a search radius of 0.″5,[8] though we note that all counterparts are found within 0.″2. Our search radius is chosen to encompass the offsets found between the optical and radio peaks (Rujopakarn et al. 2016) and is similar to the choice made in similar surveys (e.g., Guidetti et al. 2017), while the redshift cutoff is to focus our study on cosmic noon. Given the source density of 3D-HST sources and our $>4\sigma$ detection criterion, the predicted number of false detections is <0.5, i.e., negligible.[9] After one source is manually rejected owing to interference by a bright radio jet from a nearby galaxy, our final 6 GHz sample includes 100 radio sources at $z > 0.75$[10] over an area of 42 arcmin^{-2}. We then match the 3 GHz catalog (W. Rujopakarn 2020, in preparation) to this sample, finding 74 counterparts within a radius of 0.″5.

MIR and far-IR (FIR) counterparts are obtained from the Rainbow Cosmological Database through the *Rainbow Navigator* (Pérez-González et al. 2008; Barro et al. 2011a, 2011b). In the GOODS-S/CANDELS region (Grogin et al. 2011), Spitzer/MIPS 24 μm from the GOODS Legacy Program (Magnelli et al. 2009) reaches a nominal 5σ depth of 20 μJy, while the GOODS-Herschel Survey provides imaging at 70–500 μm with a 3σ depth of 2.4 mJy at 160 μm (Elbaz et al. 2011). Photometry in the Rainbow database at MIR to FIR wavelengths was performed using Spitzer/IRAC priors as described in Pérez-González et al. (2010), Barro et al. (2011a, 2011b), Rawle et al. (2016), and Rodríguez-Muñoz et al. (2019). This method of photometric extraction in principle deblends the IR photometry at the resolution of IRAC (2″); however, to be conservative, we perform a visual inspection and flag any IR fluxes as "blended" if there is evidence of multiple radio sources contributing to the 24 μm beam (6″). Of the 100 6 GHz sources, 87 are detected at 24 μm and 44 at 160 μm. A total of 11/87 MIPS counterparts are flagged as blended.

2.3. X-Ray Imaging

Our radio surveys are coincident with uniquely deep X-ray imaging from the Chandra X-ray Observatory. We utilize the 7 Ms X-ray imaging and catalog described in Luo et al. (2017), matched to our radio sample using a 2″ search radius. The full-band (0.5–7 keV), soft-band (0.5–2 keV), and hard-band (2–7 keV) catalogs have limiting fluxes of 1.9×10^{-17}, 6.4×10^{-18}, and 2.7×10^{-17} erg cm^{-2} s^{-1}, respectively. A total of 46/100 6 GHz sources are detected in at least one X-ray band, and we adopt the X-ray luminosities, hardness ratios, and source classifications as described in Luo et al. (2017).

2.4. Measured Galaxy Properties

Redshifts and stellar mass measurements are adopted from the recent grism spectroscopy release for GOODS-S from 3D-HST (v4.1.5; Momcheva et al. 2016). Redshifts are taken from the "zbest" catalogs, with the following priority: spectroscopic redshifts, robust grism redshifts, and, if the former are not available, photometric redshifts determined using the full UV −NIR photometric SED and the EAZY photometric redshift code (Brammer et al. 2008). Stellar mass measurements were derived by the 3D-HST team using the best available redshift and the full photometric data set using FAST (Kriek et al. 2009). Visual morphologies are adopted from Kartaltepe et al. (2015).

3. Radio Source Demographics

The 6 GHz luminosities can be seen as a function of redshift and stellar mass for our 100 radio sources in Figure 1. The radio luminosity was calculated assuming a typical radio spectral slope, $S_\nu \propto \nu^\alpha$ with $\alpha = -0.7$, appropriate for nonthermal synchrotron emission from star-forming regions

[8] Counterpart matching to 3D-HST catalogs is done after a systematic WCS offset correction has been applied. For more details, see Rujopakarn et al. (2016).

[9] This paper is focused on sources showing evidence of having active nuclei, further reducing any chance of false identifications (e.g., many of them have X-ray counterparts).

[10] A total of 140 6 GHz sources are matched to 3D-HST counterparts. Only the 100 at $z > 0.75$ are considered in this study.

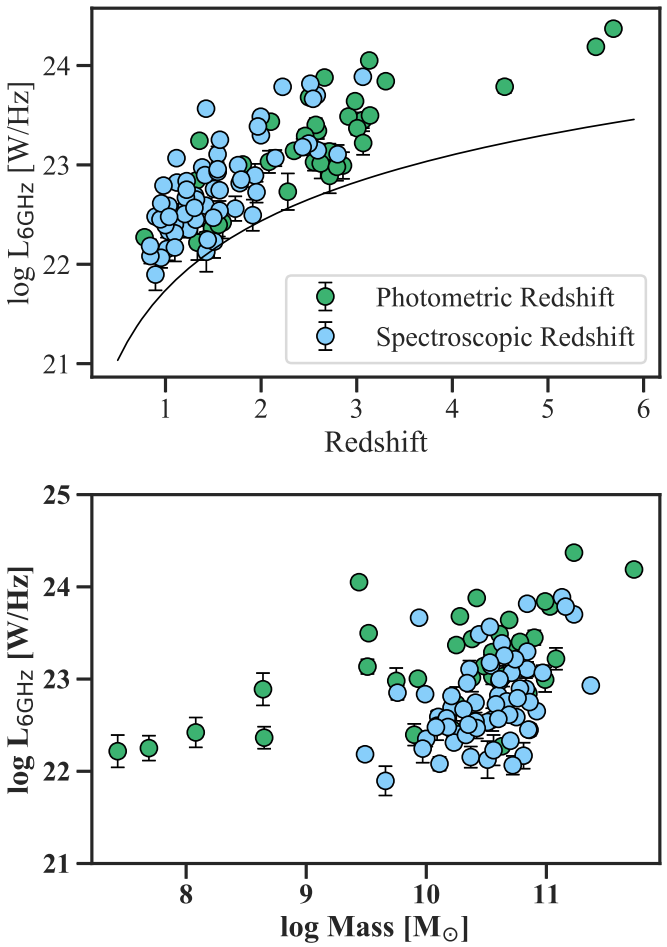

Figure 1. Rest-frame 6 GHz luminosities of our sample, assuming $\alpha = -0.7$, as a function of redshift (top) and stellar mass (bottom). Spectroscopic redshifts are indicated in blue, photometric redshifts in green. The solid line indicates the 4σ detection limit. The five cases with low ($\log M_\star/M_\odot < 9$) stellar masses have no effect on our analysis.

(Condon 1992). We utilize our 6 and 3 GHz data points to measure the true α for our sources in Section 4.4.3.

Using this convention, our radio sample spans a range of $L_{6\,\mathrm{GHz}} \sim 10^{22}$–$10^{24}$ W Hz^{-1}, consistent with the radio emission expected from (ultra)luminous infrared galaxies ((U)LIRGs) in the absence of an AGN. Most of our sample falls between $z = 0.75$ and $z \sim 3$, the former by design to focus on cosmic noon and the latter due to the positive k-correction in the radio. The sample has typical stellar masses of $\sim 10^{9.5}$–$10^{11}\,M_\odot$.

4. AGN Identification

One of our objectives is to gain as complete a census of AGN within our radio sample as possible. To do so, we identify AGN in the following ways: via X-ray properties (i.e., Lehmer et al. 2010; Xue et al. 2011); MIR excess via colors (i.e., Lacy et al. 2004; Stern et al. 2005; Alonso-Herrero et al. 2006) and SED decomposition (Assef et al. 2008, 2010; Delvecchio et al. 2017); through radio properties such as radio-loudness, a flat radio spectrum, and/or a radio morphology suggestive of jets (see Padovani et al. 2017, for a review); and of course through optical spectra. These multiple approaches are necessary to mitigate the selection biases inherent in each technique, typically stemming from obscuration or the AGN/host galaxy configuration (i.e., Juneau et al. 2011; Caputi et al. 2014; Delvecchio et al. 2017). In the following sections, we apply these criteria to our sample of radio sources to extract a comprehensive sample of AGN. An executive summary of our sample and AGN identifications can be found in Table 1, and a list of our radio sources satisfying one or more of these AGN criteria is provided in Table 2.

Table 1
Executive Summary of Our Sample and the AGN Identified by Method

Sample		
	Number	Section(s)
6 GHz (parent sample)	100	2.1, 2.2
3 GHz counterparts	74	2.2
MIPS 24 μm counterparts[a]	87	〃
PACS 160 μm counterparts	44	〃
X-ray counterparts[b]	46	2.3
Summary of AGN Identification		
Classification	Number	Section(s)
X-ray AGN[c]	31	4.1
$L_{\mathrm{x,int}} \geqslant 3 \times 10^{42}$ erg s^{-1}	23	4.1.1
Hard X-ray spectrum	11	〃
Optical spectroscopy	7	4.2
$L_{\mathrm{x,int}}/L_{6\,\mathrm{GHz}}$ Excess	38	4.1.2
MIR colors	9	4.3.1
SED fitting	14[d]	4.3.2
Radio excess	6	4.4.2
Radio flat-spectrum source	8	4.4.3
HLAGN[e]	46	5
MLAGN	3	〃

Notes. A full list is provided in Table 2. All 6 GHz sources in the parent sample are required to have a 3D-HST counterpart and be at $z > 0.75$.
[a] Eleven are determined to be blended via visual inspection (see Section 2.2).
[b] Detected in at least one X-ray band in Luo et al. (2017).
[c] Classified as AGN in Luo et al. (2017) via multiple criteria (see Section 4).
[d] Including two tentative warm-excess candidates (see Section 4.3.2).
[e] Moderate to high radiative luminosity AGN (HLAGN) and low to moderate radiative luminosity AGN (MLAGN) as defined in Delvecchio et al. (2017).

4.1. X-Ray-identified AGN

X-ray (and optical) based source classifications (galaxy or AGN) are adopted and expanded on following the criteria from Luo et al. (2017): (1) X-ray properties only, i.e., a high intrinsic X-ray luminosity and/or a hard X-ray spectrum; (2) excess X-ray relative to other multiwavelength properties, i.e., a high ratio of X-ray to the R-band, K_s-band, or radio flux; and (3) optical spectral features (see Section 4.2).

4.1.1. Selection via X-Ray Properties Only

Figure 2 shows the intrinsic (absorption corrected; see Luo et al. 2017) X-ray luminosities of our sample as a function of $L_{6\,\mathrm{GHz}}$, with hard X-ray sources highlighted. Of our 100 6 GHz radio sources, 46 are detected in the Luo et al. (2017) 7 Ms catalog, with 32 classified as X-ray AGN by that work, although one source is likely to be a misidentification resulting from blending in the X-ray and is excluded from our AGN list. The majority of these AGN are identified primarily via high intrinsic X-ray luminosity (see Luo et al. 2017 for details). The threshold for this luminosity cut varies slightly within the

Table 2
List of Radio Sources in Our 6 GHz Parent Sample at $z > 0.75$ That Satisfy One or More Criteria for AGN Identification

VLA ID	3D-HST ID	z	X-ray AGN[a]	$L_{x,int} \geqslant 3 \times 10^{42}$ (erg s^{-1})	Hard X-ray	$L_{x,int}/L_{6\ GHz}$ Excess	MIR AGN	SED AGN	Radio FSS[b]	Radio Excess	Optical Spectroscopy[c]
VLA033235.6-275021	15847	1.545	-	-	-	-			x		
VLA033231.8-274958	17069	0.99				x			x		
VLA033244.5-274940	18006	1.016	x	x	x	x					NLAGN (2)
VLA033248.6-274934	18251	1.115	x		x	x				-	
VLA033248.8-274936	18443	3.06	-	-	-	-	x	-			
VLA033235.7-274916	19348	2.582	x	x	x	x	x	x[d]			NLAGN (1)
VLA033243.5-274901	20137	1.508	x			x					
VLA033231.5-274854	20403	1.936	x	x		x					
VLA033236.0-274850	20651	1.309	x	x		x					
VLA033239.7-274850	20788	3.064	x	x	x	x	x				NLAGN (1), (2)
VLA033243.7-274851	20808	2.50	x	x		x	x	x[d]			
VLA033243.0-274845	21205	1.730	x	x	x	x					
VLA033238.7-274840	21389	2.86	x	x	x	x					
VLA033244.6-274835	21615	2.593	x	x		x		x			
VLA033241.8-274825	22154	2.10	-	-	-	-				x	
VLA033240.1-274755	24110	1.998				x					
VLA033240.3-274752	24193	3.13	-	-	-	-		x		x	
VLA033235.8-274719	26550	1.912				x			-		
VLA033222.3-274711	26650	5.68	-	-	-	-		-	x		
VLA033239.6-274709	26915	1.317	x			x			-		
VLA033228.5-274658	27882	2.515	x								
VLA033243.6-274658	28022	1.566				x					
VLA033232.5-274654	28190	1.441				x			-		
VLA033243.3-274646	28723	2.66	x	x			x	x	x	x	
VLA033230.9-274649	28743	1.173				x					
VLA033235.1-274647	28844	2.497	x			x			-		
VLA033244.0-274635	29427	2.98	x	x		x	x	x[d]			
VLA033238.5-274634	29606	2.543	x	x		x		x		-	
VLA033236.6-274631	29730	0.999				x			x	-	
VLA033246.3-274632	29816	1.220	x	x	x	x					NLAGN (2)
VLA033248.0-274626	29988	3.00	-	-	-	-	x	x[d]			
VLA033231.5-274623	30274	2.225	x	x	x	x	x	x[d]			NLAGN (1)
VLA033239.7-274611	30534	1.546	x	x		x					
VLA033223.6-274601	31240	1.033	x		x	x					
VLA033246.9-274605	31301	2.79	-	-	-	-		x	-	-	
VLA033233.0-274547	31425	0.947	x	x		x					
VLA033252.3-274542	32577	1.355				x					
VLA033230.0-274530	32932	1.221	x	x		x		x			BLAGN (1), (2)
VLA033229.9-274521	33103	0.954				x		-	-		
VLA033230.1-274523	33287	0.955	x	x		x		x		-	BLAGN (1)
VLA033229.2-274510	34114	2.59	x	x		x					
VLA033247.6-274452	35127	1.569	x			x					
VLA033238.1-274432	35774	1.221	-	-	-	-				x	
VLA033228.8-274435	36223	5.50	x	x					x		
VLA033241.0-274427	36451	1.302	x	x	x	x				x	
VLA033236.0-274424	36653	1.038				x			-		
VLA033235.1-274410	37387	0.839	x			x		x	x		
VLA033242.7-274407	37620	3.14	-	-	-	-		x	x		
VLA033229.8-274400	37885	2.08	-	-	-	-			-	x	
VLA033238.0-274400	37989	3.30	x	x		x	x	-			
VLA033241.7-274328	39751	0.979	x	x	x	x					

Notes. A dash indicates that the data were not available to assess the corresponding criteria for that source (not used for the optical spectroscopy column). In this table, $L_{x,int}$ refers to the intrinsic 0.5–7 keV X-ray luminosity.
[a] X-ray AGN as identified in Luo et al. (2017).
[b] Flat-spectrum source.
[c] NLAGN refers to high-ionization narrow-line AGN. BLAGN refers to broad-line AGN. References: (1) Santini et al. 2009; (2) Silverman et al. 2010.
[d] Warm-excess AGN candidate (Section 4.3.2).

literature, typically around $\sim 10^{42}$ erg s^{-1}, corresponding to the X-ray emission expected from the most luminous SFGs (i.e., Alexander et al. 2005). In Luo et al. (2017), a conservative threshold of $L_{0.5-7\ keV} \geqslant 3 \times 10^{42}$ erg s^{-1} is adopted (see also Xue et al. 2011; Lehmer et al. 2016). AGN meeting this criterion are shown in Table 2.

Obscured AGN can be identified via a hard X-ray spectrum (see Brandt & Alexander 2015, for a review). Both hard- and

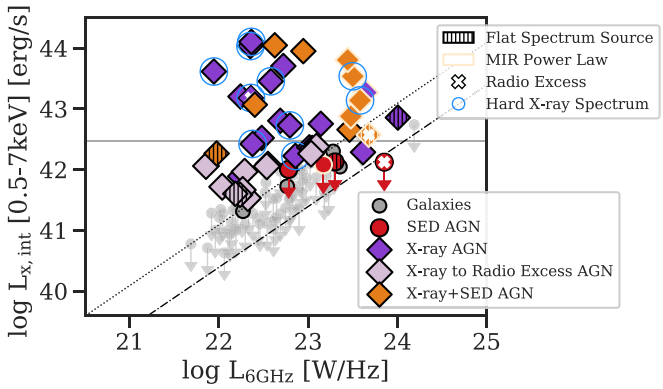

Figure 2. Intrinsic 0.5–7 keV X-ray luminosity as a function of 6 GHz luminosity (assuming $\alpha = -0.7$) for our 100 radio sources. Symbols represent AGN identified primarily via X-ray properties (dark-purple diamonds), SED fitting (red circles), or both (orange diamonds), with non-AGN galaxies shown as small gray circles. New AGN identified via their X-ray to 6 GHz excess are depicted in light purple (Section 4.1.2). Upper limits are 3σ. Additional AGN indicators are shown as follows: MIR PL emission is outlined in beige (Section 4.3.1), outliers from the radio–infrared correlation are marked with white crosses (Section 4.4.2), and flat-spectrum radio sources are denoted by vertical hatches (Section 4.4.3). Hard X-ray sources are indicated with blue circles. The dotted–dashed line denotes the nominal L_x–$L_{\rm radio}$ threshold expected for a maximal starburst. We adopt a conservative cut at 5× this level (dotted line) for the identification of AGN via excess X-ray relative to radio emission.

soft-band detections are available for about half of the X-ray detections for our radio sample. For these sources, Luo et al. (2017) measured the effective photon index, $\Gamma_{\rm eff}$. The range for our radio sample is $-1.5 < \Gamma_{\rm eff} < 2.5$, with 11 of our X-ray AGN having $\Gamma_{\rm eff} < 1.0$, indicative of an obscured AGN (see Table 2).

4.1.2. Excess X-Ray Relative to Other Properties

AGN can also be identified through excess X-ray emission relative to the output in the optical, NIR, and/or radio. As seen in Table 2, Luo et al. (2017) identified 6/31 X-ray AGN through their excess in the X-ray relative to other bands, rather than through high X-ray luminosities or hardness ratios. Here we expand on the excess X-ray to radio emission selection using our 6 GHz data, ∼9× deeper than the 1.4 GHz data employed in Luo et al. (2017).

Using the ratio of X-ray to radio for AGN identification hinges on the question of what powers the radio emission. In inactive SFGs, we can expect a relation between X-ray and radio emission, as both are dominated by mechanisms related to young SF (e.g., Vattakunnel et al. 2012). In the presence of an AGN, however, X-ray and radio emission can be sensitive to very different physical processes. The X-ray spectrum is dominated by hot coronal gas near the BH (Brandt & Alexander 2015), a ubiquitous feature in luminous AGN, modulo heavy obscuration. Radio emission, conversely, can be generated from multiple sources associated with the AGN, including, e.g., large- or small-scale jets (Gallimore et al. 2006), outflows and/or winds (Blundell & Rawlings 2001; King et al. 2013; Zakamska & Greene 2014; Nims et al. 2015), and electron acceleration within the hot corona (Laor & Behar 2008; Raginski & Laor 2016). If these mechanisms are weak or nonexistent, then radio can trace SF in the host galaxy while X-ray is dominated by the AGN (see Section 5.1 for a detailed discussion on what is powering the radio in our sample).

The L_x–$L_{\rm radio}$ relation for SFGs has been established empirically both locally (i.e., Ranalli et al. 2003, 2012; Persic & Rephaeli 2007; Lehmer et al. 2010) and at higher redshift (i.e., Vattakunnel et al. 2012) with consistent results across a range of luminosities and little evidence for redshift evolution (but see Lehmer et al. 2016). There is, however, significant (∼0.4 dex) intrinsic scatter in the L_x–SFR relation (Mineo et al. 2014; Symeonidis et al. 2014; Lehmer et al. 2016), as well as the radio–infrared correlation (0.25 dex for q_{24}; Yun et al. 2001; Rieke et al. 2009), which will propagate here. Given the L_x–$L_{\rm radio}$ relation for SFGs and the maximal X-ray emission expected for the most luminous SFGs (Alexander et al. 2005), Xue et al. (2011) and Lehmer et al. (2016) derived a threshold for excess X-ray over radio due to AGN activity as $L_{0.5\text{–}7\ \rm keV}/L_{1.4\ \rm GHz} \geqslant \beta \times 8.9 \times 10^{17}$, where β is the level of excess. To be conservative given population scatter, we adopt $\beta = 5$ and convert to $L_{6\ \rm GHz}$ using $\alpha = -0.7$, yielding $L_{0.5\text{–}7\ \rm keV}/L_{6\ \rm GHz} \geqslant 1.2 \times 10^{19}$ as our X-ray to radio excess criterion.

The X-ray to radio excess sources are indicated in Table 2. A total of 38 AGN are identified via this method, with 10 new AGN candidates based on this criterion displayed as light-purple diamonds in Figure 2.

4.2. Optical Spectroscopy

Optical spectroscopy is one of the criteria used to identify AGN in the Luo et al. (2017) source classifications, adopted in this work. The classification of AGN via optical spectroscopy falls into two categories: broad emission lines, which indicate Type 1, unobscured AGN, and highly ionized narrow emission lines, which identify Type 2, obscured AGN. Optically identified AGN in GOODS-S over the relevant redshift range were also compiled and categorized in Santini et al. (2009) and Silverman et al. (2010) from the various references therein. Matching these to our radio sample, we find that our optically selected AGN can be categorized as two broad-line AGN (BLAGN) and five narrow-line AGN (NLAGN), identified in Table 2.

4.3. Selection in the MIR

MIR colors have been shown to be effective at selecting luminous AGN, which produce a distinctive power-law (PL) spectrum in this spectral range (Lacy et al. 2004; Stern et al. 2005; Donley et al. 2012; Kirkpatrick et al. 2013). Some of these sources can be heavily obscured and are often missed in X-ray surveys (Donley et al. 2012; Del Moro et al. 2016; Delvecchio et al. 2017). Here we utilize two techniques to identify these AGN: selection in IRAC color–color space and SED fitting using the full optical–MIR photometry available from 3D-HST.

4.3.1. Selection by IRAC Colors

In Figure 3, we show the MIR colors of our radio sources, based on the Spitzer IRAC (3.6, 4.5, 5.8, 8.0 μm) bands (Lacy et al. 2004; Stern et al. 2005; Alonso-Herrero et al. 2006). A total of 13/100 of our sources are not considered for this criterion, as they do not have $>3\sigma$ measurements in all four IRAC bands and/or are at $z > 4$.[11]

[11] At $z > 4$, the IRAC bands sample stellar emission short of 1.6 μm, which can mimic an AGN PL.

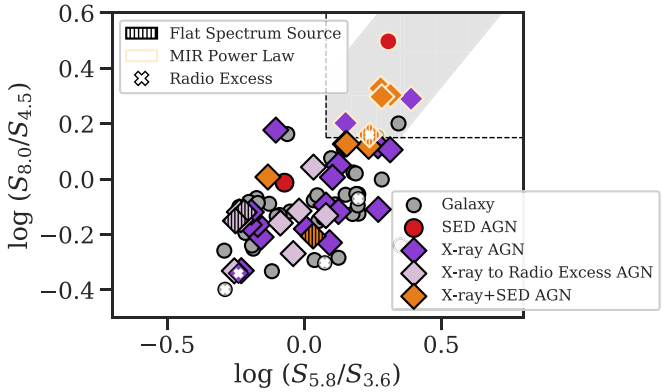

Figure 3. Spitzer/IRAC MIR colors of our radio sample, identifying PL AGN. Symbols are the same as in Figure 2. For this selection, we require a $>3\sigma$ detection in all four IRAC bands and $z < 4$ (see Section 4.3.1). We adopt the color cuts (dashed lines) from Kirkpatrick et al. (2013), designed to avoid contamination from SFGs. The shaded region denotes a similar selection from Donley et al. (2012). One non-AGN radio source (gray circles) within the shaded region is discarded as an AGN candidate owing to lack of indication of PL emission in the full SED.

We find 10 PL AGN candidates following the criteria outlined in Kirkpatrick et al. (2013), designed to minimize contamination by SFGs (see also Donley et al. 2012). Seven of these PL AGN are also identified via other selections. Of the remaining three, one is firmly an MIR PL AGN but lacks an X-ray detection or adequate photometry for SED fitting, a second is a candidate for a warm-excess AGN (see the next section), and the third is a marginal MIR color candidate with no indication of PL emission in a visual inspection of the SED. We discard the third candidate in all subsequent analysis. The MIR PL AGN are indicated in Table 2.

4.3.2. SED Fitting and Decomposition

With the extensive photometry available for most of our sources, SED fitting provides a more diagnostic approach than just using photometric colors. In this section, we describe our fitting to identify AGN that are apparent above the optical–MIR emission of the host galaxy. In addition, SED decomposition puts constraints on the fractional contribution of the AGN to the galaxy's optical–MIR emission.

For SED fitting, we require that at least nine optical–MIR photometric bands have $S/N > 3$ and `use_phot` $= 1$ in the 3D-HST catalog, indicating a robust photometric measurement. These criteria are satisfied for 91/100 of the 6 GHz radio sample. We utilize the publicly available SED fitting code from Assef et al. (2010), with modifications, to perform AGN identification and SED decomposition over the rest wavelength range 0.03–30 μm. This code performs a nonnegative linear combination of templates, applying galaxy templates first and then galaxy+AGN templates. A detailed analysis of how this method compares to other common AGN indicators was presented in Chung et al. (2014). In summary, they found that this SED fitting method identifies a population of AGN that only partially overlaps with X-ray selection and correlates well with AGN selected via optical spectroscopy. In general, this method will identify AGN that have moderate to strong contributions to optical–MIR emission independent of X-ray obscuration, but it will fail to identify AGN where the host galaxy emission dominates (see also SED3FIT from Berta et al. 2013 and subsequent studies for similar analysis).

Our template set consists of 16 star-forming spectra with variable optical attenuation ($A_v = 0$–3), representing young stellar populations; the Assef et al. (2010) "elliptical" template, representing emission from the old stellar population; and, for the AGN contribution, we adopt a standard Type 1 AGN template from Elvis et al. (1994) with host galaxy contribution removed (Xu et al. 2015b). More details of the galaxy and AGN templates used and the fitting procedure are provided in Appendices A and B. A fit with an AGN component is preferred if it is a significant improvement over a galaxy-only fit using the Fisher test, which evaluates whether an additional component or free parameter can improve a fit by chance (via the F-ratio; see Appendix A). From this test, we calculate the purity ($F_{\rm prob}$) of a sample with F-ratio larger than a given number, accounting for the relative rarity of AGN, as described in greater detail in Chung et al. (2014). We adopt a threshold of $F_{\rm prob} \geqslant 0.93$ for AGN identification. Following the fitting procedure, a visual inspection is performed on all fits.

Figure 4 (left) shows the fit for VLA033236.0-274850, indicated to be purely star-forming. Figure 4 (right) displays radio source VLA033231.5-274623, fit with galaxy templates only (top) and with galaxy+AGN templates (bottom). The latter source has $F_{\rm prob} = 0.98$—in other words, the probability that adding the AGN template improved the fit only by chance is 2%—so this source is identified as having an AGN via SED fitting. This particular example is also identified as an AGN via its X-ray properties.

SED fitting for AGN identification such as the procedure described above is limited by the currently available photometric coverage. The intrinsic spectrum of the majority of Type 1 AGN can be robustly described by the single AGN template used in these fits, empirically derived originally in Elvis et al. (1994), with modifications to remove the remaining host contamination (Xu et al. 2015b). Recent works have begun to quantify deviations from this Type 1 spectrum, revealing subpopulations of hot- and warm-dust-deficient quasars (e.g., Lyu et al. 2017), as well as contributions from line-of-sight polar dust (Lyu & Rieke 2018). Unfortunately, the constraining power of current photometric data sets to distinguish these different cases in high-redshift populations is limited due to sparse coverage of the infrared spectrum. At the typical redshifts of our sources, our long wavelength coverage consists of the IRAC and MIPS 24 μm bands, missing the crucial regions containing the stellar minimum at rest 3–5 μm and most of the 6–12 μm region, which is dominated by aromatic bands in SFGs and can probe the presence of warm dust in AGN (Lyu et al. 2017). A more detailed analysis in these cases requires additional constraints in the infrared. Similarly, these constraints will be vital to the inclusion of Type 2 templates, which we have not included here owing to the lack of convergence on simple forms of the SED suitable for our fitting procedure and available data points. For statistical samples of sources, constraining power will be provided by the 5–25.5 μm photometric coverage of JWST's Mid-Infrared Instrument (MIRI) up to $z \sim 2.5$ (see Sections 5.4–5.5 for further discussion).

Despite these limitations, we do see some indication of variety in the AGN SEDs within our sample. In five AGN with adequate photometric coverage for SED fitting, we find evidence of warm MIR excess, requiring a steeper MIR slope than can be provided by the available combinations of galaxy and the Elvis et al. (1994) template. Such warm-excess sources

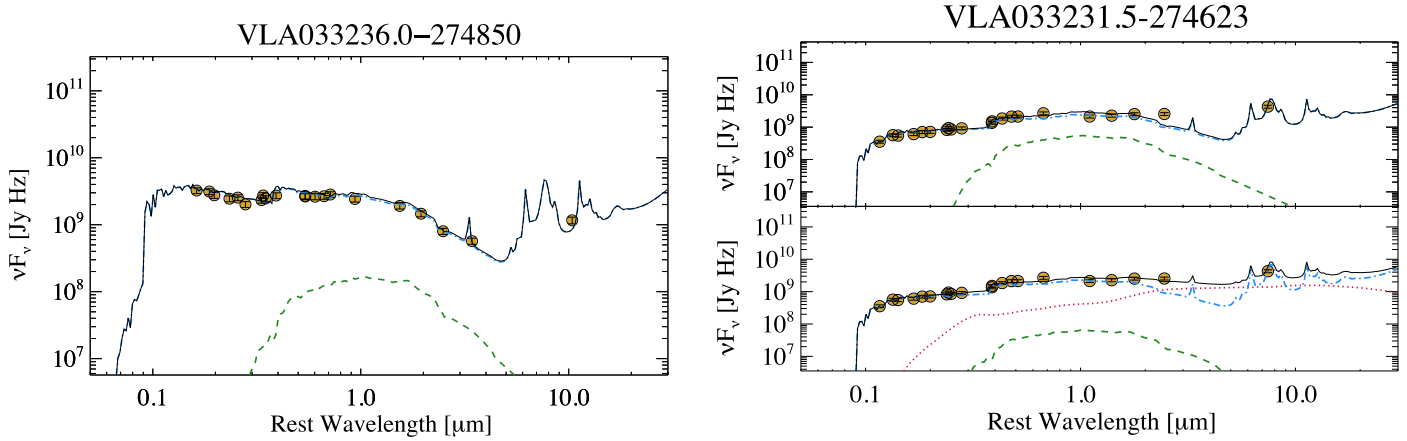

Figure 4. Left: example of the SED fit of a star-forming galaxy at $z_{\rm spec} = 1.309$. The solid black line is the total fit SED, composed of an SFG template with $A_{\rm v} = 0.6$ (blue dotted–dashed) and an old stellar population template (green dashed), fit to the observed data points (yellow circles). Right: comparison between a fit with galaxy templates only (top) and a fit with a standard Type 1 AGN template (red dotted) added (bottom) for a radio source at $z_{\rm spec} = 2.225$. The AGN template fills in the MIR excess in the region of the stellar minimum at rest ∼3–5 μm. The possibility that the AGN improves the fit only by chance is ruled out at the 98% level.

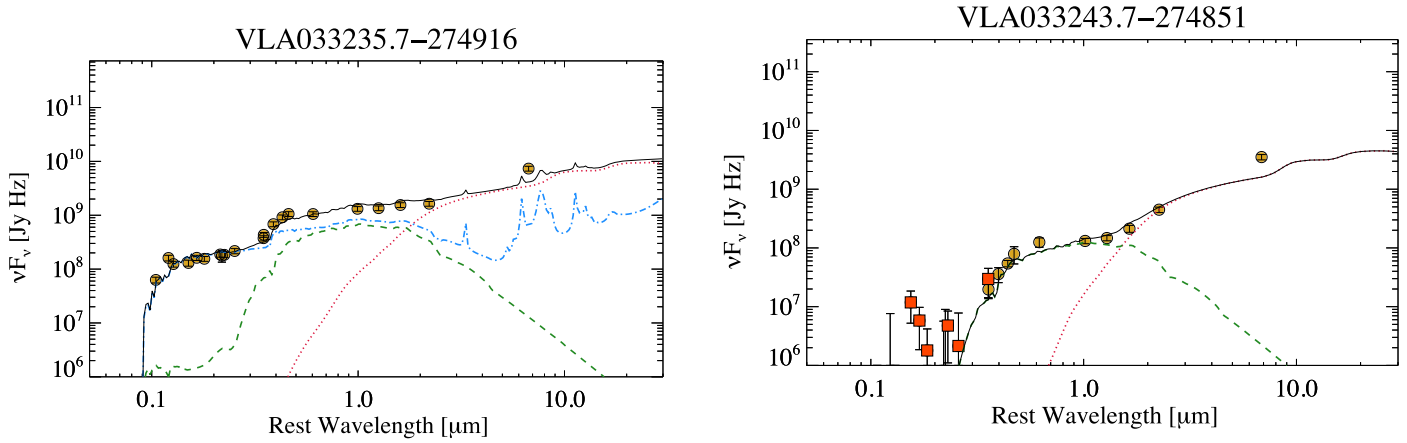

Figure 5. Two examples of MIR warm-excess AGN at $z \sim 2.5$ that are best fit with an additional obscured polar dust component, as described in Lyu & Rieke (2018). Symbols and lines are the same as in Figure 4, with red squares indicating data below the detection limit that are not included in the fit. The reddening and extra emission by polar dust result in a significantly different AGN SED, as can be seen by comparing with Figure 4 (bottom right).

have been noted in multiple AGN populations, from "normal" AGN (Kirkpatrick et al. 2015; Lyu et al. 2017) to extremely red quasars (Ross et al. 2015; Hamann et al. 2017) and hot dust-obscured galaxies (Eisenhardt et al. 2012; Wu et al. 2012). As demonstrated in Lyu & Rieke (2018), these populations can be modeled with the addition of an extended polar dust component, which adds obscuration along the line of sight to otherwise unobscured Type 1 AGN and pumps up the MIR. To test whether our warm-excess sources are better described with a polar dust component, we adopt a template from Lyu & Rieke (2018) that combines the Elvis et al. (1994) template with a polar dust component with $\tau_\nu = 3$ and redo our fits.[12] We find that 4/5 of the warm-excess candidates are better fit with the Lyu & Rieke (2018) template, with the last source degenerate between the Elvis et al. (1994) and Lyu & Rieke (2018) templates. Of the four, two (VLA033235.7-274916 and VLA033243.7-274851), shown in Figure 5, meet our threshold for an AGN ($F_{\rm prob} > 0.93$), while the other two (VLA033244.0-274635 and VLA033248.0-274626) fall just below at $F_{\rm prob} = 0.87$ and 0.88. Following the inclusion of the Lyu & Rieke (2018) template, the final median reduced χ^2 of all our fits is 2.7.

Including the two warm-excess AGN that meet our threshold, we identify 12 AGN in our radio sample via SED fitting, with an additional two tentative warm-excess candidates. One of these tentative warm-excess candidates (VLA033248.0-274626) was identified in Section 4.3.1 via MIR colors, and the other (VLA033244.0-274635) is X-ray identified. This gives us confidence that these candidates are real AGN, and we adopt the best-fit Lyu & Rieke (2018) template when deriving AGN parameters for all the warm-excess candidates. One additional AGN was robustly identified via MIR colors only (VLA033248.8-274936), lacking both an X-ray detection and adequate photometry to do SED fitting, bringing the total number of MIR AGN to 15. Of these, only 5 were not previously identified via their X-ray properties.

This high degree of overlap in X-ray and MIR selections can be compared to the overlap in a similar radio-based study from Delvecchio et al. (2017). They found that only about a third of their MIR AGN are also X-ray AGN, whereas we find that 10/15 of our MIR AGN are also identified via the X-ray. We attribute this difference to the high completeness of the 7 Ms Chandra catalog down to the lowest X-ray luminosities

[12] We note that Lyu & Rieke (2018) found that the polar dust SED is not very sensitive to the optical depth at moderate values ($\tau_\nu < 5$).

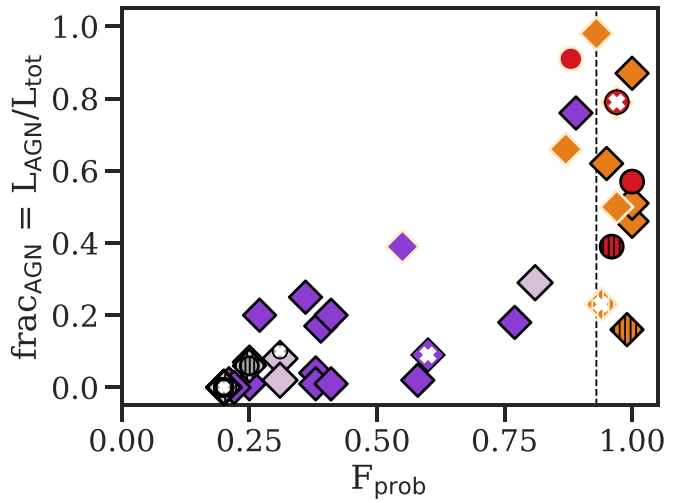

Figure 6. Fractional contribution of the AGN emission to the total optical–MIR SED derived via SED fitting, $\mathrm{frac_{AGN}}$, as a function the F-test probability, F_{prob}, that the galaxy hosts an AGN. Symbols are the same as in Figure 2. AGN identified via SED fitting have a range of AGN to host contributions, while the majority of AGN identified primarily via X-ray properties have <25% of their optical–MIR SED supplied by the AGN. The vertical dashed line denotes our selection threshold for SED-identified AGN (red circles and orange triangles); the two SED-identified AGN that fall below this threshold are warm-excess candidates.

associated with unobscured or moderately obscured AGN (10^{42} erg s^{-1} $< L_x <$ 10^{44} erg s^{-1}).

The SED fits let us compare the AGN and host galaxy luminosities. We calculate the 0.03–30 μm bolometric luminosities for the AGN and galaxy components and evaluate the AGN contribution via $\mathrm{frac_{AGN}} = L^{\mathrm{AGN}}_{0.03-30\,\mu\mathrm{m}}/L^{\mathrm{total}}_{0.03-30\,\mu\mathrm{m}}$, where $\mathrm{frac_{AGN}} = 1$ is completely AGN dominated. Figure 6 shows the fractional AGN contribution as a function of the F-test probability that the source has an AGN, where the galaxy +AGN fit results have been adopted for all AGN identified via any method. AGN identified via SED fitting have a range of $\mathrm{frac_{AGN}}$ values, indicating that this selection method is sensitive to both host- and AGN-dominated optical–MIR SEDs. The majority of AGN in our radio sample, however, are identified via X-ray properties. AGN not indicated via MIR selections are primarily host dominated, with <25% of their optical–MIR emission contributed by the AGN. For one-quarter of our full AGN sample, galaxy+AGN fits return no AGN contribution ($\mathrm{frac_{AGN}} = 0$). This result emphasizes the complementarity of the different selection techniques and shows the importance of X-ray and radio identification in finding lower-luminosity AGN that are overwhelmed by their host galaxies in the MIR.

4.4. Identification of AGN via Radio Properties

There are several metrics for identifying AGN via radio properties. In the following sections, we discuss these radio indicators of AGN activity: radio luminosity, radio morphology, outliers from the radio–infrared correlation, and flat or inverted radio spectral slopes.

4.4.1. Radio Luminosity and Morphology

RL or jetted AGN (Padovani 2016) are dominated by synchrotron emission associated with large-scale extragalactic jets. These AGN are traditionally identified via a luminosity cut, with AGN labeled RL above $L_{1.4\,\mathrm{GHz}} \gtrsim 10^{25}$ W Hz^{-1} ($L_{6\,\mathrm{GHz}} \gtrsim 10^{24.6}$ W Hz^{-1}; Miller et al. 1990). Morphological signatures can also identify RL AGN, as kiloparsec-scale extragalactic jets can be easily recognized in radio images with sufficient resolution. Neither a straight luminosity cut nor visual morphological selection is considered a complete selection, however, and so it is common in the literature to also examine the radio emission in relation to other portions of the SED; for example, the X-ray-to-radio ratio (Terashima & Wilson 2003), the optical-to-radio ratio (Kellermann et al. 1998), and the radio–infrared correlation (Helou et al. 1985; Condon et al. 1991; Yun et al. 2001).

Our radio sample falls entirely below the traditional RL AGN luminosity cut (assuming $\alpha = -0.7$; Figure 1). This is consistent with a visual inspection of our subarcsecond-resolution 6 GHz radio image, which reveals no evidence of large-scale extragalactic jets. These base-level checks, together with the fact that RL AGN are relatively rare ($\lesssim$10%–20%; Bonzini et al. 2013; Williams & Röttgering 2015), suggest that there should be few or even no RL AGN in our sample. In the next section, we expand our search for RL AGN via the radio–infrared correlation, using the q_{24} parameter (Donley et al. 2005; Bonzini et al. 2013). These AGN may be missed by nonradio indicators owing to the AGN being in a phase of less efficient BH accretion (Delvecchio et al. 2017).

4.4.2. The Radio–IR Correlation

The goal of this section is to identify RL AGN via outliers from the well-established radio–infrared correlation for SFGs (Helou et al. 1985; Condon et al. 1991; Yun et al. 2001), which holds over a wide range of luminosities and has a weak, if any, dependence on redshift (Ivison et al. 2010; Mao et al. 2011; Magnelli et al. 2015; Delhaize et al. 2017). This relation is typically evaluated via the q-parameter, the ratio of infrared, via MIR, FIR, or total infrared emission, to the 1.4 GHz radio emission. To match the depth of our radio observations in the infrared as well as possible, we adopt $q_{24,\mathrm{obs}} = \log(S_{24,\mathrm{obs}}/S_{1.4\,\mathrm{GHz,obs}})$, where $S_{24,\mathrm{obs}}$ is the observed MIPS 24 μm flux density and $S_{1.4\,\mathrm{GHz,obs}}$ is the 1.4 GHz flux density (Appleton et al. 2004; Donley et al. 2005; Bonzini et al. 2013). We use q_{24} rather than q_{160}, q_{250}, or FIR luminosity because FIR counterparts are only detected for approximately half our radio sample; these are utilized later in the discussion to explore the origin of radio emission (see Section 5.1.1).

Deriving the 1.4 GHz flux density requires that we extrapolate from 6 GHz, under the assumption that the 1.4–6 GHz radio spectrum can be described as a PL. Recent works by Delhaize et al. (2017) and Tisanić et al. (2019) evaluated the sensitivity of the SFG locus of the radio–IR correlation to the assumed radio spectral slope, α. They found that, although different assumptions for α can affect the normalization and redshift dependence of the SFG locus, the effect is small (at the ~20% level for the derived luminosity; Tisanić et al. 2019) in comparison to the intrinsic scatter in the relation. Therefore, we assume the fiducial value of $\alpha = -0.7$ when deriving the 1.4 GHz flux density from 6 GHz, with the caveat that we may misclassify sources with extreme slopes.

Figure 7 shows $q_{24,\mathrm{obs}}$ for our sample up to $z \sim 3$, the highest redshift where 24 μm traces SF activity. To define an SFG locus, we extract $q_{24,\mathrm{obs}}$ over $0 < z < 3$ from a set of local representative SFG templates from Rieke et al. (2009) at log $L_{\mathrm{IR}}/L_{\odot} = [11, 11.5, 12]$. These templates form a reasonable

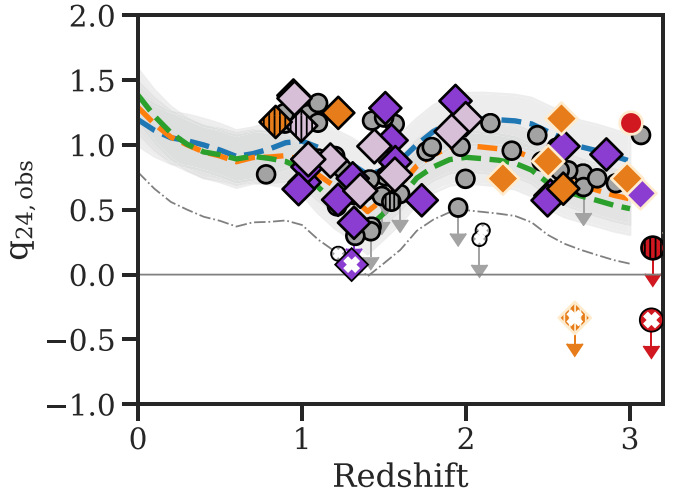

Figure 7. Radio–infrared correlation for the full radio sample. Symbols are the same as in Figure 2. The dashed lines indicate representative SFG templates (Rieke et al. 2009; Rujopakarn et al. 2013) at $\log L_{IR}/L_{\odot} = [11, 11.5, 12]$, with an assumed 0.2 dex scatter (shaded region). The dotted–dashed line marks our criterion for an outlier, 0.5 dex below the midpoint of the SFG locus as defined by the templates; a source below this line is classified as an RL AGN. This criterion is applied up to $z = 3$, where the 24 μm band probes SF. The solid line indicates the canonical cut at $q_{24,obs} = 0$ adopted in previous studies (Donley et al. 2005).

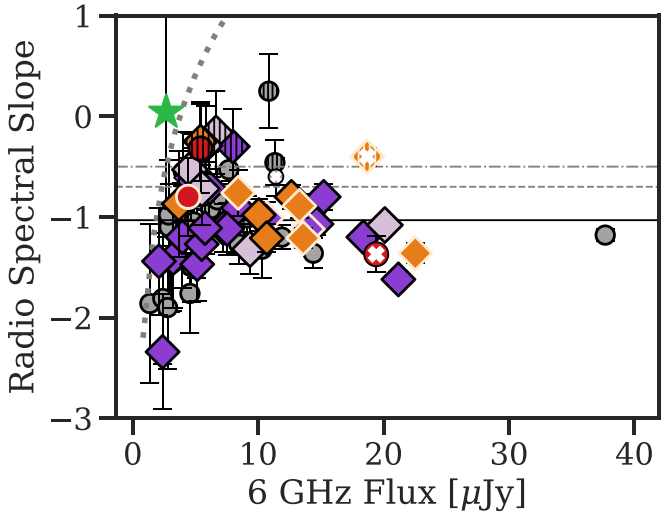

Figure 8. Radio spectral slope of our sources as a function of their 6 GHz flux densities. Symbols are the same as in Figure 2. The dotted line indicates our sensitivity limit for the radio slope based on the shallower 3 GHz data. The green star is the stack of the 26 sources not detected at 3 GHz. The solid line indicates the average slope of our radio sample with detections at both 3 and 6 GHz. The dashed line indicates the canonical $\alpha = -0.7$ slope for SFGs (Condon 1992), while the dotted–dashed line indicates the boundary for flat-spectrum AGN $\alpha \geqslant -0.5$ (i.e., Padovani 2016; Padovani et al. 2017).

basis for infrared-bright SFGs with a scatter of ∼0.2 dex in SFR (Rieke et al. 2009) up to $z \sim 3$ (Rujopakarn et al. 2013; De Rossi et al. 2018). We define an outlier from this distribution as being 0.5 dex below the midpoint of this locus (which is approximately represented by the $\log L_{IR}/L_{\odot} = 11.5$ template; Figure 7). This method is adopted as recent works have shown that previous uses of q_{24} in the literature, such as adopting a threshold ($q_{24,obs} < 0$; Donley et al. 2005) or an archetypal template (M82; Bonzini et al. 2013), can result in significant incompleteness (Del Moro et al. 2013; Delvecchio et al. 2017). Using this criterion, we identify three sources with radio excess relative to the SFG $q_{24,obs}$, one of which is also an X-ray-identified AGN.

As noted in Section 2.2, 11/100 of our sources are blended at the resolution of MIPS and so excluded from this analysis. An additional 13 radio sources are undetected in MIPS. We evaluate these sources for radio-loudness by estimating their 3σ upper limits. The GOODS-S 24 μm map has a nominal rms of 4 μJy; however, at this depth, confusion noise will drive the achievable detection limit. As discussed in Dole et al. (2004), confusion noise is a function of local source density and beam size, raising detection limits at this depth by 2.5–3 times the instrument noise. For our data, an accurate source position was used as a prior, resulting in a slightly smaller confusion noise component. As the local confusion limit is difficult to estimate quantitatively, we assume a factor of two times the rms level and show the $3\sigma_{conf}$ upper limits in Figure 7. We find three MIPS-undetected radio sources that are indicated to be RL AGN. Two of these sources were already identified as AGN; of these, VLA033243.3-274646 was already known to be an outlier from the correlation, via ALMA observations (Rujopakarn et al. 2018). The third, VLA033229.8-274400, is more tentative; it is a weak (∼4σ) detection at 6 GHz with a marginally constraining MIPS upper limit indicating radio excess. We include it in our sample but caution that confirmation is needed. The radio excess sources are listed in Table 2.

4.4.3. The Radio Spectral Slope

In the previous two sections, we examined our radio sample for indications of RL AGN activity. The majority of AGN, however, are RQ and have radio emission that originates from SF and/or the AGN via, e.g., small-scale jets or outflows. In both the RL and RQ populations, an AGN embedded in a compact, optically thick radio core will experience synchrotron self-absorption (Rybicki & Lightman 1986), which will flatten the radio slope relative to that from SF or an optically thin AGN. This provides a relatively clean AGN selection, with radio slopes $\alpha \geqslant -0.5$, termed "flat-spectrum source" (FSS) AGN (e.g., Wall & Cooke 1975; Peacock & Gull 1981; Willott et al. 2001; Kimball & Ivezić 2008; Massardi et al. 2011; Padovani 2016; Padovani et al. 2017).

In this section, we measure the radio spectral slope, α, assuming a PL spectrum using our (observed) 3 and 6 GHz photometry for the 74 sources that have detections in both bands. Although the beam size differs by up to a factor of ∼2 between our radio bands, Gim et al. (2019) show that we can expect this to have a minimal effect on our determination of the spectral slopes, further mitigated by our use of tapering. However, requiring a detection in both bands will bias us against flat radio slopes, and observational limitations may result in artificially steepened slopes; we discuss these potential biases in the next section. The majority of our sources are at $0.75 < z < 3$, which corresponds to a rest frequency range of 5–24 GHz. Figure 8 shows our derived radio spectral slopes as a function of the 6 GHz flux. We find that sources detected in both bands have $\langle\alpha\rangle = -1.0 \pm 0.5$, an average that is consistent within the scatter with the canonical value of $\alpha = -0.7$ (Condon 1992) and in good agreement with recent works that find a steep ($\alpha \sim -1$) slope at high frequencies (Tisanić et al. 2019).

For the quarter of our sources not detected at 3 GHz, we measure an average radio slope by performing median stacking on the 3 GHz image using the publicly available code

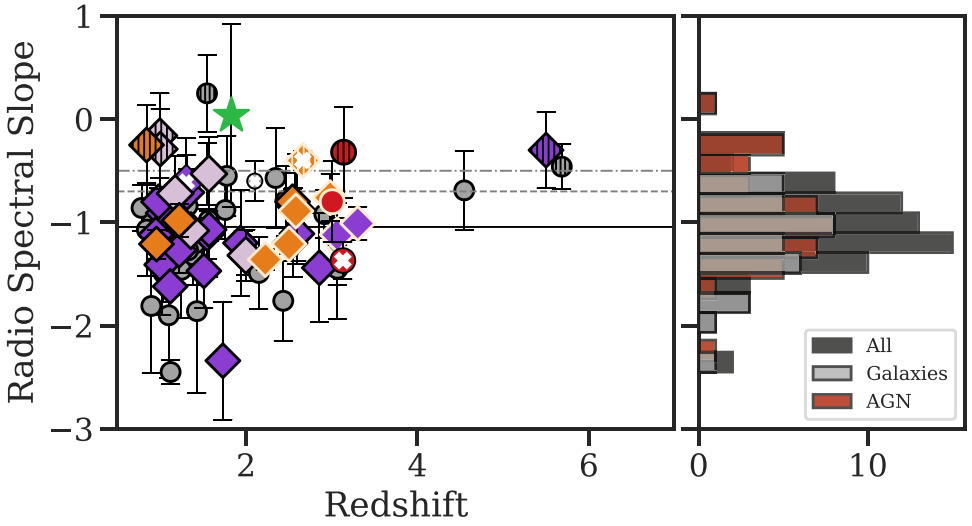

Figure 9. Left: radio spectral slope as a function of redshift. Symbols are the same as in Figure 2. The green star is the stack of the 26 sources not detected at 3 GHz. Lines are the same as in Figure 8. Right: histogram of all radio sources (black), those classified as galaxies (gray), and those classified as AGN (red). There is no significant difference in the average slope of the galaxy and AGN 3 GHz detected subsamples.

`Stacker` (Lindroos et al. 2015). We find that the 6 GHz sources undetected at 3 GHz have a stacked flux density of $S_{3\,\mathrm{GHz}} = 1.8 \pm 0.4\,\mu$Jy. The stacked error has been increased by 20% owing to stacking on the image rather than in the *uv*-plane, as suggested in Lindroos et al. (2015). The resulting slope based on the stacked 3 GHz and the median 6 GHz photometry can be seen as the star in Figures 8 and 9. On average, our sources undetected at 3 GHz fall just below the detection limit. They may have shallower slopes than the rest of our sample, although the result differs from an on-average steep spectrum by only $\sim 2\sigma$ and needs to be refined with deeper radio data at 3 GHz, which will be presented in future work.

Though low-redshift studies over a comparable frequency range have recently found a significant fraction of FSS AGN within luminous Seyfert and LINER populations (Zajaček et al. 2019), the expected fraction of FFS AGN is not yet well constrained, particularly in the *faint* RQ regime. Our analysis reveals eight FSS AGN candidates (Table 2), six of which were previously identified as AGN and one of which is RL. This number is likely a lower limit, as the depth of the 3 GHz data biases our analysis against flat radio slopes (see Section 4.4.4). In Figure 9, we look at the distribution of radio slopes as a function of redshift, finding no redshift dependence, and break the radio spectral slopes into galaxy and AGN subpopulations. We find that, minus the FSS AGN, the average slopes are identical, $\langle\alpha\rangle = -1.1 \pm 0.4$. The source of the radio emission is discussed further in Section 5.

Given that our observations are at high rest-frame frequencies, we consider whether our flat radio spectral indices could be produced by mechanisms unrelated to AGN activity. At $\nu \gtrsim 10$ GHz, it is expected that free–free emission plays an increasingly important role, adding a flat ($\alpha_{\mathrm{ff}} = -0.1$) thermal component to the steeper synchrotron spectrum that dominates at lower frequencies (Klein et al. 1988; Condon 1992; Tabatabaei et al. 2017). This effect would make the identification of AGN via a flat spectrum more ambiguous with our data. In practice, however, a flattening of the radio spectral slope is not observed in high-redshift SFGs. As mentioned earlier, Tisanić et al. (2019) recently showed that, for a sample of SFGs (SFR $> 10\,M_{\odot}$ yr^{-1}) up to $z \sim 4$, the average rest-frame 0.5–15 GHz radio SED is best described by a broken PL with a steep ($\alpha \sim -1$) slope at high frequencies (rest $\nu > 4.3$ GHz). A detailed analysis of 14 local SFGs by Klein et al. (2018) using radio data up through 24.5 GHz provides a closer look at this behavior. First, low-mass, low-luminosity galaxies do indeed have a large free–free component in their GHz radio spectra, but the fraction drops substantially for massive, luminous galaxies (such as those in our sample; see also Clemens et al. 2008; Leroy et al. 2011). Second, the best-fit nonthermal spectra for their massive galaxies *all* steepened toward high frequencies, and in a way that preserves the general PL slope despite the presence of a significant free–free component. We are therefore confident that free–free emission is unlikely to mimic a flat-spectrum AGN in our data.

4.4.4. Observational Biases toward Steeper Slopes

Observational limitations of our data sets may result in (1) the inability to measure a slope for radio sources with relatively flat radio spectra and/or (2) the artificial steepening of the slopes we do measure. The first effect stems from the depth of the 3 GHz data, which is of order two times shallower than the 6 GHz survey. Requiring a detection in both bands to measure the radio spectral index produces a bias against flatter radio spectra. In the previous section, we demonstrated that the stacked 3 GHz flux density of 3 GHz undetected sources lies just below our detection limit on average, indicating that the fraction of FSS AGN identified in this study is likely a lower limit.

Artificial steepening of the measured slopes may, on the other hand, result from the underestimation of the true flux density owing to an inability to recover emission on scales that are poorly sampled by the current *uv*-coverage. This effect will disproportionately affect our 6 GHz imaging, which has a factor of two higher resolution than that at 3 GHz. Recent work by Gim et al. (2019) demonstrated that measuring the radio spectral slope based on radio imaging surveys with significantly different resolutions can greatly increase the scatter in the measured slopes. While our resolution difference is in a range where they find only a minimal increase in scatter, we test for this effect by looking at our radio spectral slopes as a function of the ratio between the 6 GHz peak radio flux from

the native resolution map and the total radio flux after tapering (see Section 2.1). For compact or point sources, this ratio will be 1. If extended sources are preferentially having flux resolved out at 6 GHz, we should see steeper slopes for more extended sources. From this test, we ascertain that there is no correlation between radio slope and this proxy for source compactness in our data.

While the above test gives us confidence in our measured photometry for extended sources, we cannot entirely rule out a frequency-dependent underestimation of the radio fluxes, as tapering cannot recover faint, diffuse emission in the case of extremely poor *uv*-coverage. A simple test was performed to look for a correlation between radio spectral slope and the S/N of the 6 GHz detections. Steeper slopes at low S/N would potentially indicate losses due to poorly covered baselines; we find no such trend in our data.

We highlight one additional secondary effect that may affect our data: in this work, we have utilized the multiterm multifrequency synthesis (MT-MFS) algorithm to account for the frequency-dependent sky brightness of our broadband data and the *w*-projection algorithm to correct for wide-field errors caused by non-coplanar baselines. This is followed by a post-deconvolution wideband primary beam correction. We note that this imaging strategy does not correct the second-order flux and spectral index errors caused by the rotation of the primary beam pattern of the VLA antennae with time (the so-called *A*-terms). These uncorrelated direction-dependent primary beam errors are known to cause an artificial steepening of source spectral indices by approximately -0.1 ± 0.2 at the half-power point of the primary beam (Rau et al. 2016). A more advanced, but currently computationally prohibitive, strategy that would reduce the artificial spectral index steepening would be to employ the full *aw*-projection algorithm (Jagannathan et al. 2018). A more rigorous elimination of the potential spectral index limitations and biases discussed in this section will require additional observations with shorter baselines at 6 GHz and the application of a more advanced algorithm. For this work, we stress that in spite of the caveats discussed in this section, our imaging strategy is sufficient to establish an interesting lower limit on the occurrence of FSS AGN signatures.

4.5. X-Ray AGN without Radio Detections

To assess fully the source density of known AGN in the ultradeep VLA area, we expand our search to include X-ray-identified AGN in the Luo et al. (2017) catalog that are radio undetected. For these X-ray AGN, in addition to having no radio counterpart, we impose the same criteria as in Section 2.1, namely, $z > 0.75$ and an optical/NIR counterpart in the CANDELS/3D-HST catalog, identified by Luo et al. (2017) using their likelihood-based counterpart matching. We find 57 radio-undetected X-ray AGN.

5. Discussion

In the preceding sections, we have applied a multiwavelength approach to identify AGN in a radio-selected sample from ultradeep X-ray, optical–MIR, and radio imaging. We identified AGN in fully half ($51\% \pm 10\%$) of our sample of 100 radio sources. Thanks to ultradeep X-ray imaging with high completeness (Luo et al. 2017), the majority of these AGN (41/51 or ∼80%) have some AGN signature in the X-ray: an X-ray luminosity indicative of an AGN, a hard X-ray spectrum, and/or an excess in X-ray to optical, NIR, or radio emission. AGN are additionally identified through MIR excess, using MIR colors and optical–MIR SED fitting, and through radio properties.

Our parent sample is based on ultradeep, high-resolution radio imaging covering 42 arcmin^{-2} and so consists of faint radio sources mainly in the μJy regime, $S_{6\,\mathrm{GHz}} \sim 1$–$40\,\mu$Jy, corresponding to $S_{1.4\,\mathrm{GHz}} \sim 3$–$110\,\mu$Jy assuming a standard $\alpha = -0.7$ slope. It is the first opportunity to probe the radio properties of AGN at this faint level, reaching 4–10× deeper than comparable studies. In the EDCF-S region, which encompasses the GOODS-S/HUDF region and our survey, deep VLA 1.4 GHz measurements (Seymour et al. 2004; Miller et al. 2013) enabled multiple studies of AGN in radio populations down to detection limits of $S_{1.4\,\mathrm{GHz}} \sim 30$–$40\,\mu$Jy. Utilizing infrared and radio properties to identify AGN, Seymour et al. (2008) measured an AGN fraction of $28\% \pm 8\%$. Later work included X-ray and $q_{24,\mathrm{obs}}$ indicators, finding an AGN fraction of $43\% \pm 4\%$ (Bonzini et al. 2013; Padovani et al. 2015). A direct comparison requires a few caveats: our sample is restricted in redshift range ($z > 0.75$) and covers a smaller area, biasing us against rarer, luminous sources. Nevertheless, our result is in good agreement with the latter studies at 1.4 GHz, demonstrating that the AGN fraction remains substantial at fainter radio fluxes.

We similarly compare to recent results from the VLA-COSMOS 3 GHz Large Project, which reaches a detection limit equivalent to $S_{1.4\,\mathrm{GHz}} \sim 20\,\mu$Jy (Delvecchio et al. 2017; Smolčić et al. 2017). AGN in this 3 GHz survey were subdivided into two categories: moderate to high radiative luminosity AGN (HLAGN) and low to moderate radiative luminosity AGN (MLAGN), where luminosity refers to the AGN luminosity and is a proxy for the radiative efficiency of BH accretion (Delvecchio et al. 2017). The former are identified via X-ray, MIR, and/or optical–MIR SED fitting, while the latter are radio excess AGN that are not also HLAGN. Using the COSMOS 3 GHz sample, Delvecchio et al. (2017) identified 21% of the sample as HLAGN and 17% as MLAGN. By contrast, we find that $46\% \pm 10\%$ of our AGN are HLAGN and only $3\% \pm 10\%$ of them are MLAGN (Table 1). This difference is likely primarily due to the completeness of X-ray data available in the GOODS-S/HUDF, highlighting the importance of ultradeep X-ray in not only identifying but characterizing AGN. We can also compare the fraction of HLAGN with radio excess: ∼30% for the COSMOS sample and only ∼7% in our survey, possibly due to the smaller area covered and depth of our radio imaging. If we expand the classifications presented above to include any radio signature (radio excess *and* flat radio spectra), then our numbers increase slightly to 5% MLAGN and 17% HLAGN with radio excess and/or a flat radio spectrum; however, it is unclear that these signatures should be grouped in terms of the represented mode of BH accretion (Whittam et al. 2017).

In the following sections, we first discuss the majority of our AGN sample to address what is powering the radio emission in RQ AGN. We then turn the discussion to AGN that are indicated directly via radio indicators, i.e., radio-loudness and a flat or inverted radio spectral slope. Finally, we discuss a number of items that pertain to the future possibilities for improving our understanding of the overall AGN population.

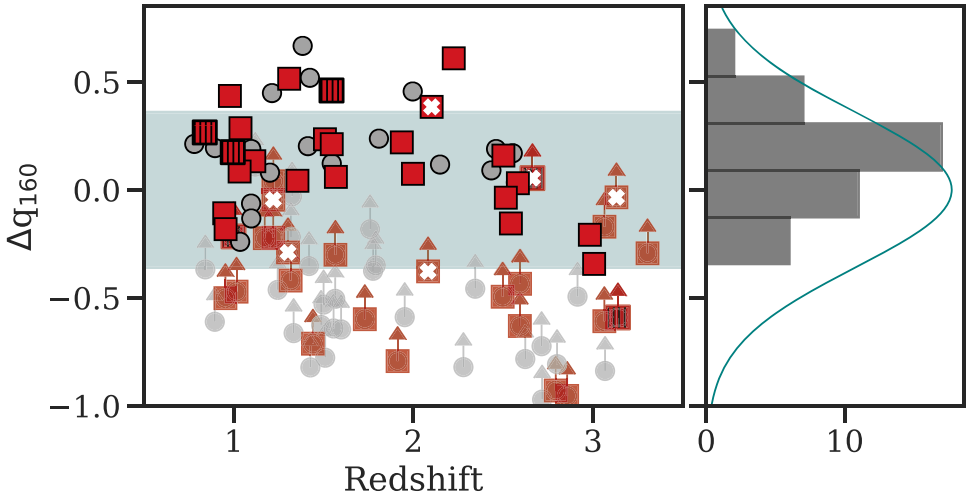

Figure 10. Left: deviation, Δq_{160}, of the radio–infrared correlation at 160 μm for our radio sources from a fiducial SFG template (Section 5.1.1) as a function of redshift (three sources at $z > 3.5$ are not shown for clarity). The symbols show AGN (red squares) and galaxies (gray circles), with 3σ lower limits. FSS and RL AGN are indicated as in Figure 2. The shaded region denotes the 1σ scatter found in local populations (Yun et al. 2001; Qiu et al. 2017). Right: histogram of Δq_{160} for all detected sources. The overlaid Gaussian is normalized (not fit) to the maximum height of the histogram, centered on zero with the local scatter.

5.1. The Origin of Radio Emission in High-z, Radio-quiet AGN

The radio emission of faint RQ AGN at high redshift is thought to be dominated by SF. Modeling suggests that SFGs dominate the total 1.4 GHz counts below ~100 μJy (Mancuso et al. 2017), or correspondingly below $L_{6\,\mathrm{GHz}} \sim 10^{23.5}\,L_{\odot}$ at $z \sim 2.5$. Radio stacking of X-ray-identified AGN supports this conclusion (Pierce et al. 2011). Our study, however, is the first instance where this question can be probed with radio data sufficiently sensitive to *detect* typical SFGs at $1 \leqslant z \leqslant 3$ (Madau & Dickinson 2014). In the following sections we approach the question of the source of radio emission in AGN by (1) investigating whether the radio flux densities are as expected for SFGs, (2) showing that typical RQ AGN are not expected to contribute significantly to the radio at these flux densities, and (3) showing that the galaxy morphologies are typical for SFGs. From these analyses, we conclude that, indeed, the radio emission of AGN in our sample is dominated by the SF in their host galaxies.

5.1.1. Radio–Infrared Relation for SFGs at 160 μm

In addition to identifying outliers, the radio–infrared relation can be used to test whether radio flux densities are consistent with originating from SF activity. In Section 4.4.2, we utilized 24 μm measurements to look for outliers since this band matches the radio depth as closely as possible; here, we focus on measurements at observed 160 μm, as this wavelength regime is dominated by dust heated by SF over the entire redshift range of interest ($1 \lesssim z \lesssim 3$), with little to no contribution from AGN emission (i.e., Kirkpatrick et al. 2013).

Approximately half of our radio sample is detected at 160 μm, a rate expected owing to the incompleteness driven by confusion noise in the Herschel data at these flux levels (Berta et al. 2013). For this subsample, we first determine $q_{160}^{6\,\mathrm{GHz}} = \log(S_{160,\mathrm{obs}}/S_{6\,\mathrm{GHz,obs}})$. For upper limits on the remaining sources, we adopt a detection limit of 5.2 mJy, which corresponds to the 80% completeness for this field (Berta et al. 2011). We find that our sample has a distribution with a standard deviation of 0.35 dex.

For comparison, we use a fiducial SFG: the log $L_{\mathrm{IR}}/L_{\odot} = 11.5$ template of Rieke et al. (2009). This template has been shown to be representative of the SEDs of infrared galaxies at $1 < z < 3$, the redshift range of our sample (Rujopakarn et al. 2013; De Rossi et al. 2018). To check the appropriateness of our fiducial model, we compare the $q_{160}^{1.4\,\mathrm{GHz}}$ derived from the template to an SFG sample from Mao et al. (2011), adjusting their q_{70} using a color correction from our fiducial Rieke et al. (2009) template. We find that the log $L_{\mathrm{IR}}/L_{\odot} = 11.5$ template well represents the Mao et al. (2011) sample. We therefore use the template to generate redshift-dependent values of $q_{160,\mathrm{fiducual}}^{1.4\,\mathrm{GHz}}$, which we correct from 1.4 to 6 GHz assuming a radio spectrum of $\alpha = -0.8$ to obtain $q_{160,\mathrm{fiducual}}^{6\,\mathrm{GHz}}$ (=2.71, 2.67, 2.38 at $z = 1, 2, 3$, respectively).[13] To determine the width of the distribution around $q_{160,\mathrm{fiducial}}^{6\,\mathrm{GHz}}$, we evaluate the distributions for local, high-metallicity galaxies for $q_{160}^{1.4\,\mathrm{GHz}}$ from Qiu et al. (2017) and for $q_{60}^{1.4\,\mathrm{GHz}}$ from Yun et al. (2001). At $z \sim 0$, these two wavelengths (160 and 60 μm) roughly bracket the rest wavelength range for observed 160 μm for our sample. We find a virtually identical width to that for the high-redshift galaxies, with a standard deviation of 0.36 dex.

We show the distribution of values for the GOODS-S sample compared with the predicted values determined from the log $L_{\mathrm{IR}}/L_{\odot} = 11.5$ template in Figure 10, where $\Delta q_{160} = q_{160,\mathrm{fiducial}}^{6\,\mathrm{GHz}} - q_{160,\mathrm{obs}}^{6\,\mathrm{GHz}}$. Sources that fall significantly above the Δq_{160} distribution would have excess radio relative to their 160 μm emission. The shaded region denotes $\pm$ the standard deviation found in local galaxies (Yun et al. 2001; Qiu et al. 2017), which is also displayed as a Gaussian distribution in comparison to the 160 μm detected sources in the right panel. The Gaussian has been normalized to the height of the source histogram but not otherwise fit to the data. It is nevertheless in good agreement, with a slight asymmetry that is likely due to the nondetections at 160 μm. That is, the behavior of Δq_{160} for our sample appears to be consistent with the scatter for radio emission powered purely by SF.

[13] The full redshift dependence of $q_{160,\mathrm{fiducial}}^{6\,\mathrm{GHz}}$ for $0.7 < z < 3.4$ can be reproduced using the following polynomial: $2.79 - 0.516 \times z + 0.748 \times z^2 - 0.367 \times z^3 + 0.0533 \times z^4$.

As discussed in Section 4.4.2, a typical criterion for an RL AGN is that its ratio of infrared to radio should be a factor of 10 or more lower than the typical value for SFGs; we have shown that none of the 160 μm detected subsample falls into this category. However, we cannot rule out radio excess among the lower limits, and, indeed, the majority of the RL AGN identified previously via their q_{24} are found in this subsample. However, our q_{24} analysis shows that RL AGN are rare. Therefore, we conclude that if the 160 μm emission from these galaxies is powered as expected purely by SF (and thereby 160 μm nondetections are not biased toward or against radio excess from AGN), then most of the radio emission probably has the same origin. This behavior is consistent with that of brighter RQ or more descriptively nonjetted AGN (Padovani 2016), which often have FIR-to-radio ratios similar to those for SFGs, leading to the belief that their radio outputs are dominated by SF (e.g., Heckman & Best 2014).

5.1.2. Radio Output of Nonjetted (Radio-quiet) Quasars

It is still possible within the scatter of the SFG radio–infrared relation to find an AGN that contributes significantly to the total radio emission. However, we show in this section that the radio output from an AGN in our galaxies is likely to fall considerably below the output from SF. For this purpose, we determine the radio–infrared nonjetted, radio-quiet quasars (RQQs) in the sample of White et al. (2017), which they demonstrate has sufficiently luminous AGN to dominate (>50%) in the radio.

The sources in the White et al. (2017) sample have measurements at 1.4 GHz (VLA), 160 μm (Herschel), and 24 μm (Spitzer). In addition, all targets are at a single epoch ($z \sim 1$), simplifying k-corrections. For this sample, the Spitzer 24 μm observations probe rest 12 μm, which can be a good measure of both the total AGN luminosity (Spinoglio & Malkan 1989) and SF activity (Rujopakarn et al. 2013). Although we expect the 24 μm outputs of these sources to be dominated by the output of the AGN, SF can still make a contribution. We estimate this contribution as follows. We assume that the flux density at 160 μm is entirely due to SF and, using the Rieke et al. (2009) log $L_{\rm IR}/L_{\odot} = 11.5$ template, determine that the ratio of flux density at 160 to 24 μm should be ~60 at $z \sim 1$ for purely stellar-powered outputs. With this estimate, we can remove the SF component from the flux density of the RQQs at 24 μm by removing 1/60 of that observed at 160 μm to get an estimate of the portion due *only* to the AGN.

From the values with the SF contribution removed, we compute $q_{24,\rm AGN}^{1.4\ \rm GHz} = \log\ (S_{24\ \mu\rm m,AGN}/S_{1.4\ \rm GHz})$ for the AGN component of each source, obtaining a lower limit for the cases not detected in the radio. We utilize all targets with 1.4 GHz measurements with S/N $\geqslant 2$ and adopt 2σ upper limits for the rest. The average for the White et al. (2017) quasar sample (including lower limits that are >1.5) is $q_{24\mu\rm m,AGN}^{1.4\rm GHz} = 1.7$, with a median of 1.8. Three quasars from White et al. (2017) stand out as having low values of $q_{24}^{1.4\ \rm GHz}$ and may be radio intermediate. If we cut them from the sample, the average and median both become 1.8. These values can be compared with $q_{24}^{1.4\ \rm GHz} = 1.0$ for purely SFGs at $z \sim 1$. That is, for nonjetted AGN the radio flux density at rest 3 GHz is 5–6 times weaker relative to the output at rest 12 μm than is the case for purely SFGs. To the extent that both AGN and SF radio spectra are optically thin synchrotron spectra with similar slopes, this conclusion will hold roughly independent of radio frequency.

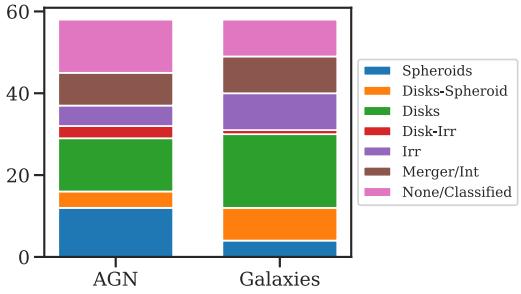

Figure 11. Breakdown of the visually classified stellar morphologies (Kartaltepe et al. 2015) for our AGN and galaxy subsamples for the full faint radio population. Stellar morphology classifications include spheroids, disks, and irregular (irr) galaxies, as well as subclasses combining those dominant classes. None/unclassified includes sources where the source morphology could not be classified. Sources are also flagged for potential merger or interaction activity; as this flag was in addition to the morphological classification, sources can be double counted in this representation.

Since the rest 12 μm output of an SFG is correlated with its bolometric infrared luminosity, we can conclude that the radio output due to AGN activity in the majority of our ultrafaint radio sample is generally significantly smaller than the radio emission due to SF.

5.1.3. NIR Morphologies

To assess the morphologies of the host galaxies for our AGN sample, we adopt the visually classified NIR morphologies from Kartaltepe et al. (2015). These morphologies are based primarily on *H*-band imaging, with supplementary information from *V*- and *I*-band images, and are assessed by multiple classifiers. The visual classification catalog includes multiple image depths; when possible, to be sensitive to disturbed morphologies, we adopt the classification in the deepest image. Galaxies are classified into dominant types: spheroidal (including compact/point sources), disks, and peculiar/irregular, with combinations of these types possible, or none/unclassifiable. Sources with signs of merger or interaction activity are flagged separately (see Kartaltepe et al. 2015, for more details). Figure 11 shows the breakdown in our AGN and galaxy subsamples by visually classified morphology. Overall, the morphology distribution is similar between the two subgroups, with AGN showing a slight preference for spheroidal hosts (by a factor of 3 ± 1.7). Mergers and interactions make up a minority, ~15%, in both the AGN and galaxy subsamples, suggesting no excess in disturbed morphologies associated with AGN activity. Keeping in mind sample size, we find no particular trend of morphology or interaction signature in our AGN sample, consistent with the hosts being comparable to the SFG population.

5.2. AGN Indicators in Faint Radio Sources: Radio-loud and Flat-spectrum AGN

In this work, we have identified RL AGN as outliers from the radio–IR correlation (Section 4.4.2), as well as both RL and RQ AGN as flat-spectrum sources over the observed 3–6 GHz radio SED. Within the overall AGN population, RL AGN are a minority ($\lesssim$10%–20%; Bonzini et al. 2013; Williams & Röttgering 2015) and are typically associated with lower-redshift, massive BHs at the centers of early-type galaxies. Within our sample, we find 6/51 (~12%) RL candidates with a range of redshifts ($z \sim$ 1–3), radio fluxes and spectral slopes,

stellar masses (log $M_\star/M_\odot \sim 9.5$–11), and morphologies. Half of our RL candidates are based on upper limits at 24 μm, suggesting that they may reside in hosts with lower SF, though we find that their visual morphologies are likely not early type as is typical at lower redshifts. The overlap of radio-loudness with other AGN indicators is mixed: three are identified solely through radio excess, while the other three have X-ray and/or MIR signatures (see Table 2). One RL AGN is additionally an FSS AGN candidate.

The remainder of our AGN sample is RQ, with seven RQ AGN showing a direct indication of AGN activity through a flat radio spectrum. Five of these FSS AGN are identified as AGN through multiple indicators, giving us confidence that they are bona fide AGN (Table 2). The remaining two are tentative; even though SFGs at these redshifts show little evidence of free–free emission flattening out the radio spectrum at these frequencies (Tisanić et al. 2019), we cannot completely rule out nonobvious mechanisms that could mimic an AGN with a flat radio spectrum.

We can compare the fraction of FSS AGN (8/51 or $\sim$16% $\pm$ 6%) in our faint radio sample to those from wider but shallower ATCA 5.5 GHz imaging in the GOODS-S field. There, Huynh et al. (2015) found that 39% $\pm$ 7% of AGN with 50 μJy $< S_{5.5\mathrm{GHz}} <$ 100 μJy had a flat or inverted 1.4–5.5 GHz slope. Similarly, Gim et al. (2019) found a fraction of 30% $\pm$ 8% with slopes $\geqslant -0.5$, in a radio sample largely fainter than 100 μJy at 5.5 GHz. These fractions of FSS AGN are higher than ours by $\sim 2.5\sigma$. This difference may in part be due to the quarter of our sample not detected at 3 GHz, which stacking suggests contains additional FSS AGN (Section 4.4.3). Deeper 3 GHz imaging, to be presented in future work, will test this possibility.

Although it may be coincidental, the fractions found in faint radio populations (Huynh et al. 2015; Gim et al. 2019) are similar to those for FSS AGN in much brighter samples, observed at similar frequencies (e.g., Wall & Peacock 1985; Zajaček et al. 2019). These bright sources are generally associated with highly active AGN, e.g., blazars. The nature of the faint FSS AGN need not be analogous, but they are likely to be associated with an active nucleus (Gim et al. 2019). Extrapolations to low flux density radio AGN in empirically based simulations suggest increasing core fractions with decreasing AGN luminosity, resulting in increasing numbers of FSS AGN due to, e.g., synchrotron self-absorption (Whittam et al. 2017). This and the apparent uniformity of the fraction of FSS AGN suggest that flat radio spectra are useful indications of AGN activity across a broad range of radio flux densities. However, at faint levels the AGN nature of the candidates will need confirmation, and the analysis must guard against contamination by free–free emission.

In summary, out of 51 AGN in a radio-selected sample, about one-third have a direct indication of AGN activity in their radio properties. This reiterates the need for a multiwavelength approach in identifying AGN with current data sets and is consistent with radio emission in the μJy regime being mostly associated with SF in the host, which was addressed in detail in the previous section.

5.3. The Source Density of AGN at Cosmic Noon

While submillijansky radio-selected samples provide additional constraining information in a regime probing both SFG and AGN populations, the requirement of a radio detection introduces a bias against RQ AGN in more quiescent hosts. This bias is confirmed by the 57 additional AGN candidates found via their X-ray properties (Luo et al. 2017) that are not detected in our radio data (Section 4.5).

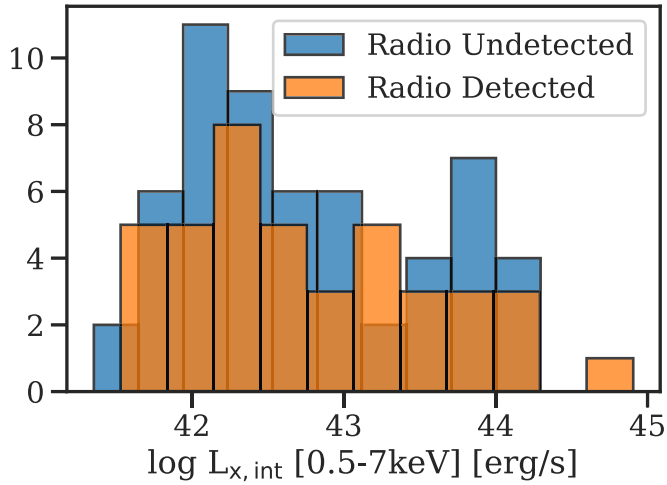

Figure 12. Histogram showing the intrinsic X-ray luminosity for both radio-detected (orange) and radio-undetected (blue) AGN samples.

The distributions of the intrinsic X-ray luminosities for our radio-detected and radio-undetected AGN samples can be seen in Figure 12; the distributions are qualitatively similar. Together the radio-selected sample of AGN and the radio-undetected X-ray AGN imply a source density of at least 2.6 arcmin^{-2} at cosmic noon above $S_{0.5-7\,\mathrm{keV}} \sim 4 \times 10^{-17}$ erg s^{-1} cm^{-2}. This does not include potential MIR excess AGN within the radio-undetected population; however, as demonstrated in Section 4.3.2, the majority of AGN identified ($\sim$80%) have an AGN signature in the X-ray, due to the ultradeep X-ray available in the HUDF. An additional missing population, heavily obscured AGN, will be discussed in the following sections.

5.4. A Census of AGN: Have We Found Them All?

The primary goal of this work is to compile as complete a census of AGN activity as possible in an area of ultradeep legacy surveys, using a multiwavelength approach, with results summarized in Tables 1–2, Section 5, and Section 5.3. In this section, we assess a particularly elusive AGN population that is almost certainly still underrepresented: heavily obscured AGN. We describe the nature of these objects, discuss future possibilities for their identification, and estimate the possible yields of such sources.

5.4.1. Obscured AGN in This Work

Obtaining a complete sample of AGN has been known to be a significant challenge for years. Every search method finds only a fraction, as is made clear, for example, by the Venn diagram in Delvecchio et al. (2017), the lack of edge-on galaxies in optically selected samples (Maiolino & Rieke 1995), the failure of infrared methods to find all X-ray-bright AGN (Donley et al. 2008), and the failure of some infrared-identified AGN to be detected even with very deep X-ray data (Del Moro et al. 2016, this work). In our study, the fraction of AGN found *only* in the MIR is small relative to the X-ray identifications, compared with the results of previous studies (e.g., Donley et al. 2008; Delvecchio et al. 2017). This

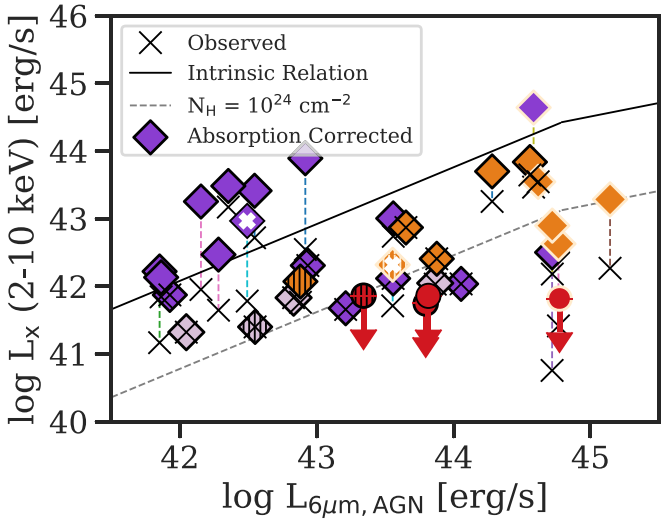

Figure 13. Rest-frame 2–10 keV X-ray luminosity as a function of the rest 6 μm luminosity of the AGN for our AGN that have sufficient photometry for SED fitting. The full symbols are the same as in Figure 2 for the absorption-corrected, intrinsic X-ray luminosity (see Luo et al. 2017), which are connected by dashed lines to crosses showing the uncorrected, observed X-ray luminosity. The solid line indicates the intrinsic (unobscured) relation from Chen et al. (2017). The dashed line is this relation obscured by a column density of $N_H = 10^{24}$ cm^{-1}; AGN below this line are in the Compton-thick regime.

difference is possibly because of the extremely deep X-ray data available in the GOODS-S/HUDF field. However, the use of MIR SED fitting to identify AGN is *also* currently limited not only by the available photometric coverage but also by our understanding of the full range of diversity in intrinsic AGN spectra. As discussed in Section 4.3.2 and Appendix A, we limit our SED fitting primarily to a single Type 1 AGN template. Because of the broad range of SED predictions for type 2 circumnuclear tori, we have not been able to include them in the fitting.

This omission produces a bias prohibiting a complete census of obscured AGN. Alternative techniques can somewhat make up for this bias; obscured AGN are revealed in our sample as 11 AGN with hard X-ray spectra, the 9 MIR PL AGN, and the handful of optical spectroscopic confirmations of high-ionization narrow emission lines, which indicate Type 2. To assess more accurately the fraction of moderately and heavily obscured AGN in our sample, we utilize the well-established correlation between the intrinsic X-ray luminosity and the NIR emission of the AGN (i.e., Fiore et al. 2009; Gandhi et al. 2009; Del Moro et al. 2016; Chen et al. 2017), here determined at rest 6 μm from the best-fit AGN template (Figure 13). To compare to the relations established in the literature, we derive the rest 2–10 keV X-ray luminosity using the `Sherpa` Python package (Freeman et al. 2001). We then compare to the intrinsic relation derived in Chen et al. (2017). We additionally compare to this relation given a factor of 20 in attenuation of the X-ray emission, corresponding to a column density of $N_H = 10^{24}$ cm^{-1} erg s^{-1} (Lansbury et al. 2015, 2017); this column density marks the Compton-thick (CT) regime.

We find that our AGN largely scatter around the intrinsic relation, as expected, but with signs of increasing obscuration at higher 6 μm luminosities. About 30% of our AGN are consistent with being heavily obscured or Compton-thick, which is within the range of predicted CT fractions (~10%–50%; e.g., Treister et al. 2009; Akylas et al. 2012). This range is, however, poorly constrained, as estimates of the CT fraction currently rely on X-ray observations, which suffer from degeneracies between obscuration and the X-ray reflection component (Akylas et al. 2016; Georgantopoulos & Akylas 2019).

5.4.2. The Bimodal Obscured AGN Population

The most elusive AGN are those with Compton-thick absorbing columns, such as those found in the SWIFT-BAT survey by Akylas et al. (2016). To understand the prospects for finding a more complete sample of Compton-thick AGN at higher redshifts, we need to understand their nature. The BAT sample seems to include two types. The first is cases where we view the AGN almost exactly edge-on and the high column is because we are looking edge-wise through the circumnuclear torus. A good example is NGC 5728, studied in detail by Durré & Mould (2018). Their measurements show two prominent ionization cones in [O III], very symmetric in appearance. At their apices is the core of the reflected X-ray emission that is also distributed symmetrically, as well as the peak of the radio emission. The second case is where the AGN is deeply embedded and its energy is largely absorbed and reradiated in the infrared. In extreme absorbed cases, the energy of the AGN is completely thermalized and emerges as a ~300 K blackbody-like spectrum, albeit with the effects of radiative transfer, such as strong silicate absorption. Mrk 231 and IRAS 08572+3915 are two possible examples (Armus et al. 2007). It is beyond the scope of this paper to test the prevalence of these two types in the BAT sample, but it appears that both types are well represented.

However, one must be careful not to oversimplify any classification scheme. As an illustration, Mrk 231 is apparently not Compton-thick from the NuSTAR spectrum, with $N_H = 1.2 \times 10^{23}$ cm^{-2} (Teng et al. 2014). However, its nuclear SED in the infrared strongly suggests a pseudo-blackbody, as expected if nearly all of its energy has been absorbed, and its complete lack of MIR emission lines (Armus et al. 2007) is consistent with this hypothesis. Teng et al. (2014) suggest that the lack of lines is due to an intrinsically weak UV and X-ray continuum, but the lack of *all* lines, including, for example, all of the forbidden neon lines with ionization potentials ranging from 21.6 eV ([Ne II]) to 126 eV ([Ne VI]), and of other bright MIR fine-structure lines having even lower values (e.g., 15.8 eV for [Ar II], only slightly more than for hydrogen, 13.6 eV), makes this explanation unlikely. It seems more plausible that the circumnuclear material is highly clumpy and that our line of sight is relatively unobscured but not representative of the average obscuration over 4π sr, i.e., the source could be Compton-thick viewed from most directions but not in ours.

In any case, the example of Mrk 231 shows that the infrared behavior may not track exactly that in the X-ray, i.e., sources classified as Compton-thin (albeit with a substantial atomic column) from the X-ray spectrum might have the great majority of their luminosity absorbed by circumnuclear material, so that it emerges in the MIR. Such sources, heavily absorbed and underluminous in the X-ray (Teng et al. 2014), would be underrepresented in X-ray-selected samples, as would bona fide Compton-thick sources. In the following discussion we will describe the two types of behavior as "absorbed" and "edge-on" to avoid any reference to specific X-ray properties.

We first consider the absorbed case. The bolometric luminosity of Type 1 AGN is an order of magnitude greater than their 0.5–10 keV luminosity (Lusso et al. 2012). That is, an AGN with an X-ray luminosity $\geqslant 3 \times 10^{42}$ ergs s^{-1} should have a bolometric luminosity $\geqslant 10^{10}$ $L_{\odot}$. AGN templates—those representing both Type 1 (e.g., Fritz et al. 2006) and Type 2 (e.g., Nenkova et al. 2008), the latter of which have been shown to fit partially obscured AGN relatively well (see González-Martín et al. 2019b)—indicate that the SED of these cases is broad but generally peaked near 10 μm, as demonstrated in the examples of Mrk 231 and IRAS 08572+3915. That is, the energy will emerge primarily in the MIR and the SED will extend with considerable strength into the 3–5 μm range.

To make this point quantitative, we take Mrk 231 as the prototype for an absorbed AGN. Adopting the relation between bulge and BH mass from Kormendy & Ho (2013), Equation (2), and taking the K–W2 color of a galaxy bulge to be 0.24 (from Willner et al. 1984 plus our own calculation of W1–W2 for a large sample of elliptical galaxies), we derive

$$\log(L_{\rm Edd}/L_{\odot}) = 13.239 - 0.484(M_{\rm W2} + 24.45), \quad (1)$$

where $L_{\rm Edd}$ is the Eddington luminosity of an average-mass BH (according to the Magorrian relation) in a galaxy bulge of absolute magnitude $M_{\rm W2}$. The distance modulus of Mrk 231 is 36.38 and Wide-field Infrared Survey Explorer (WISE) measures W2 = 6.301, so its $M_{\rm W2} = -30.1$. From Cutri et al. (1984) and the standard K–W2 color, the *stellar* $M_{\rm W2} = -25.9$, i.e., it can be ignored relative to the total at this band. The AGN luminosity is $\log L_{\rm AGN}/L_{\odot} = 12.05$ (Farrah et al. 2003), whereas Equation (1) gives $\log L_{\rm Edd}/L_{\odot} = 13.94$. That is, the luminosity of the AGN is slightly more than 1% of the Eddington luminosity corresponding to an average supermassive BH in a galaxy of the stellar brightness of the Mrk 231 host. The AGN is, however, about 4.2 mag brighter at 4.5 μm than is the host galaxy, i.e., BHs emitting at $\geqslant$0.03% of $L_{\rm Edd}$ with this luminosity absorbed by circumnuclear material should be identifiable through the excess emission at 4.5 μm. This result should hold down into the Seyfert galaxy range, i.e., to AGN luminosities of $\sim 10^{10} L_{\odot}$.

We now consider the edge-on situation. There is a broad extinction minimum between 3 and 8 μm (Xue et al. 2016), where the nominal optical depths are similar to those at 6–8 keV in the X-ray (Corrales et al. 2016). Reverberation mapping demonstrates that the infrared emission in this range originates at the inner rim of the circumnuclear torus, which is ~0.1–2 pc in diameter depending on the AGN luminosity (Lyu et al. 2019), whereas the X-ray source is expected to be extremely compact. Therefore, for a clumpy circumnuclear torus the 3–8 μm infrared emission can escape along the relatively less obscured lines of sight over an extended region, and hence can escape more readily than is typical for the 6–8 keV X-ray emission, given equal nominal optical depths. It is just in the 6–8 keV range that Compton-thick AGN are revealed (Georgantopoulos & Akylas 2019). This situation underlies one of the arguments that it should be possible to find "hidden" AGN in the MIR.

To make a quantitative estimate, we take the "normal" quasar template of Lyu et al. (2017). If there is no extinction in the circumnuclear torus and the emission of its inner rim at 4.5 μm is isotropic, the threshold for detection of the emission as an excess above the galaxy stellar spectrum is of order 0.1% of $L_{\rm Edd}$, again assuming the average supermassive BH via the Magorrian relation and using the measurements of Mrk 231 to set a conservative threshold. The zero extinction assumption is probably optimistic, but the assumption of isotropic emission is probably roughly correct. Assuming a net extinction of a factor of 10, the threshold is ~1% of $L_{\rm Edd}$.

5.5. Future Detection Possibilities

The Mid-Infrared Instrument on JWST will be very effective at finding absorbed AGN and also useful for edge-on ones, as illustrated by the estimates above. The multiple spectral bands in MIRI are well suited to probing galaxy SEDs for AGN activity up to $z \sim 2.5$ (Messias et al. 2012; Kirkpatrick et al. 2017), with sufficient spectral resolution to isolate the 4–5.5 μm region that is a minimum in SFGs, even those with prominent aromatic features. A pilot program will be conducted by the US MIRI Guaranteed Time Observation (GTO) team (PI: G. Rieke) covering about 30 square arcmin in the GOODS-S/HUDF field overlapping with the deep VLA field discussed in this paper. The integration times have been set to obtain roughly equal S/N in the MIRI bands for a ν^{-2} PL between 5.6 and 21 μm (excluding the filter at 11.3 μm). At rest 6 μm, this pilot survey will reach 5σ depths of 2 μJy (6 μJy) at $z \sim 1$ ($z \sim 2$) in the F1280W (F1800W) filter. Via the $L_x - L_{6\,\mu{\rm m}}$ relation (i.e., Chen et al. 2017), this corresponds to an X-ray flux limit of $S_{0.5\text{–}7\ {\rm keV}} \sim 5 \times 10^{-16}$ erg s^{-1} cm^2 ($\log L_{[0.5\text{–}7\ {\rm keV}]}/{\rm erg\ s^{-1}} \sim 42.3$) at $z \sim 1$, assuming an unabsorbed X-ray source with $\Gamma = 1.4$. As an example, we should achieve S/Ns in all these bands of $\gtrsim$10:1 for sources with spectra similar to Mrk 231 but only 1% as bright at $z = 1$ (i.e., bolometric luminosity of $\sim 10^{10} L_{\odot}$) and only 10% as bright at $z = 2$ (i.e., bolometric luminosity of $\sim 10^{11} L_{\odot}$).

From the source density found in this study, we therefore expect to detect a minimum of ~50 AGN in this survey at cosmic noon. Given the ability to detect AGN down to 1% of Eddington as previously discussed, the counts for obscured and/or low-luminosity AGN may increase this number: recent work using infrared color diagnostics suggests a larger fraction of AGN among the IR population detectable by MIRI, driven mainly by AGN–host composites with strong host emission in the low Eddington ratio regime (Kirkpatrick et al. 2017). Our MIRI GTO survey will test these predictions. Taking our conservative estimate and the possible range of the fraction of Compton-thick AGN of 12%–30% of the total number of AGN (Akylas et al. 2016), and assuming that half are absorbed, we then expect to find at least three to eight examples in this survey, plus additional detections of edge-on cases. Of course, it is possible that more (or less) examples will be found, depending on the properties of the AGN population. Future MIRI surveys of larger areas are important to improve the statistics regarding this population.

Are there other detection approaches? The S/N in the NuSTAR data (e.g., Georgantopoulos & Akylas 2019) on the relatively nearby BAT sample indicates that using hard X-rays to characterize the distant population of Compton-thick and related AGN is beyond current technical capabilities. However, there are two additional possibilities. The first is to look for variability in the 3–5 μm region; rms fluctuations of ~7% seem to be characteristic (Lyu et al. 2019). The second is to search

for galaxies with ratios of [O III] λ5007 to Hβ strongly indicative of an AGN but with no other indications. Such cases are candidates for edge-on systems with large columns of absorbing material from their circumnuclear disks.

6. Conclusions

This work presents an analysis of AGN in faint radio populations based on new, deep radio imaging at 6 (0.32 μJy rms, $0\farcs31 \times 0\farcs61$) and 3 GHz (0.75 μJy rms, $0\farcs6 \times 1\farcs2$) in the GOODS-S/HUDF region. Combining these with existing deep legacy data sets, we apply AGN identification techniques in the X-ray, optical–MIR, and radio to assess the AGN fraction and nature of AGN in a faint ($S_{1.4\,\mathrm{GHz}} \sim$ 3–100 μJy equivalent) radio sample. Our main conclusions are as follows:

1. Within our 100 radio sources at $z > 0.75$, we find that 51 are AGN candidates via one or multiple AGN indicators. The majority (80%) of our AGN are indicated via X-ray properties; the uniquely deep 7 Ms X-ray available in this field provides high completeness at the X-ray luminosities expected of moderately luminous AGN ($L_x \sim 10^{42}$ erg s^{-1}). A total of 15/51 have MIR excess, determined via MIR colors and/or SED fitting, including five candidates for warm-excess AGN, which may indicate a polar dust component (i.e., Lyu & Rieke 2018). A total of 6/51 have radio excess, indicating RL AGN activity, and at least 8/51 have flat or inverted radio spectral slopes over 3–6 GHz, indicating compact radio cores. Additional flat-spectrum source AGN are likely among the 3 GHz undetected subset as indicated by stacking; it is plausible that flat radio spectra are as prevalent in our faint sample as found in brighter radio populations, making this a useful AGN indicator. Deeper 3 GHz imaging to test this possibility will be presented in future work.
2. In sources where radio emission is predominately from SF activity, the X-ray-to-radio ratio provides a robust method for AGN identification. Even given a conservative criterion of 5 times the maximal X-ray emission for a starburst (Section 4.1.2), combined deep X-ray and radio data yield 38/51 AGN identified via this method, 10 of which are not otherwise indicated by more traditional X-ray criteria, i.e., luminosity or X-ray hardness.
3. In good agreement with comparable studies (4–10$\times$ shallower than our survey; Bonzini et al. 2013; Delvecchio et al. 2017; Ceraj et al. 2018), we determine that the radio output of our very faint RQ AGN is largely consistent with originating from SF activity. Comparing the radio–infrared ratio at 160 μm of our AGN and SFG subsamples to a fiducial SFG template (Rieke et al. 2009) recovers the local radio–infrared correlation for SFGs including the measured scatter from local samples. This result is supported by the similar distributions of the radio spectral index between AGN and SFGs (minus FSS AGN) and by the comparable host morphologies and interaction rates between the two subsamples. We further demonstrate via a sample of luminous RQ (or nonjetted) quasars (White et al. 2017) that for truly RQ AGN, the output in the radio due to AGN activity is likely 5–6 times lower relative to the MIR than that expected from SF.
4. In addition to the 51 AGN in the radio-selected sample, 57 radio-undetected AGN are indicated via X-ray properties in the relevant area and redshift range. Combined, these AGN populations indicate an AGN source density of at least 2.6 arcmin^{-2} at cosmic noon above $S_{0.5-7\,\mathrm{keV}} \sim 4 \times 10^{-17}$ erg s^{-1} cm^{-2}. This result is a lower limit given biases in our analysis against FSS AGN and heavily obscured or Compton-thick AGN.
5. Despite the success of multiwavelength identification of AGN, a potentially substantial population of AGN, i.e., Compton-thick AGN, remains elusive. Within our radio sample, we find that $\sim$30% are likely heavily obscured despite several biases against these sources in our selection techniques, i.e., relatively soft band X-ray observations and the assumption of a Type 1 AGN template during SED fitting. We discuss the nature of the potentially still missing Compton-thick AGN population, considering two likely cases of "absorbed" and "edge-on" configurations. We show that in both cases coverage of the rest 4–5.5 μm region will provide a clear signature of AGN activity above the ubiquitous stellar minimum in inactive galaxies, down to $\sim$0.03% and $\sim$1% of L_{Edd} in "absorbed" and "edge-on" cases, respectively. Coverage of these wavelengths will be provided by JWST/MIRI up to $z \sim 2.5$.

The authors thank Jianwei Lyu and Benjamin Johnson for insights into SED fitting and Pablo Pérez-González for discussions on the Rainbow Database. The National Radio Astronomy Observatory is a facility of the National Science Foundation operated under cooperative agreement by Associated Universities, Inc. Basic research in radio astronomy at the U.S. Naval Research Laboratory is supported by 6.1 Base Funding. This research has made use of data obtained from the Chandra Data Archive and the Chandra Source Catalog and software provided by the Chandra X-ray Center (CXC) in the application packages CIAO, ChIPS, and Sherpa. This work is based on observations taken by the 3D-HST Treasury Program (HST-GO-12177 and HST-GO-12328) with the NASA/ESA Hubble Space Telescope, which is operated by the Association of Universities for Research in Astronomy, Inc., under NASA contract NAS5-26555. This work has further made use of the Rainbow Cosmological Surveys Database, which is operated by the Centro de Astrobiología (CAB/INTA), partnered with the University of California Observatories at Santa Cruz (UCO/Lick,UCSC). Additionally, this work has made use of ASTROPY, a community-developed core Python package for astronomy (Astropy Collaboration et al. 2013) hosted at http://www.astropy.org/.

Appendix A
SED Fitting Details

SED fitting is performed using a nonnegative linear combination of a small set of representative templates (Assef et al. 2008, 2010; Chung et al. 2014; Alberts et al. 2016). The templates include an elliptical model, representing the old stellar population, star-forming models for young stellar populations, and an optional AGN component. During fitting, a prior is applied to the R-band luminosity, empirically determined via data from the Las Campanas Redshift Survey (Lin et al. 1996), to avoid unphysical fits (Assef et al. 2010). The IGM absorption is fixed as a function of

redshift (Assef et al. 2010; Chung et al. 2014). Additional reddening of the AGN template is allowed as a free parameter.

The Assef et al. (2010) SED fitting code comes prepackaged with empirically derived galaxy and AGN templates. However, likely because our galaxies were selected in a different manner than the original Assef et al. (2010) sample, we find that these galaxy+AGN templates do not provide robust fits. We make the following substitutions. For galaxy templates, we replace the "spiral" and "irregular" templates with a series of 16 spectra with variable optical attenuation ($A_v = 0$–3) generated using the Flexible Stellar Population Synthesis code (FSPS; Conroy et al. 2009; Conroy & Gunn 2010). For more details on these spectra, see Appendix B. These star-forming spectra are then combined with the Assef et al. (2010) "elliptical" template, to allow for a variable old stellar population contribution relative to emission from young stars. The best fit of a single FSPS spectra + elliptical template is then adopted as the host galaxy fit. Figure 4 shows an example.

After fitting the stellar-based templates, we refit all sources with an added AGN template. Here we adopt the empirical X-ray-radio AGN template presented in Elvis et al. (1994), modified to remove the host galaxy FIR contribution (Xu et al. 2015b). The Elvis et al. (1994) template supplies the intrinsic optical–MIR SED of a luminous Type 1 AGN (see also Richards et al. 2006; Elvis et al. 2012; Scott & Stewart 2014; Lyu et al. 2016, 2017; Lyu & Rieke 2017), which has been shown to be applicable to AGN and quasars over a range of redshifts (Jiang et al. 2006, 2010; Xu et al. 2015b), and properties such as Eddington ratio (Hao et al. 2011, 2014). Reddening of the AGN template is allowed to vary as a free parameter. This approach does not include Type 2 AGN, which are expected to be just as prevalent. Unfortunately, the SEDs of Type 2 AGN have yet to be robustly constrained, with Type 2 circumnuclear tori models producing a wide range of potential SEDs with strong degeneracies (see Ramos Almeida & Ricci 2017; González-Martín et al. 2019a, 2019b). The photometric constraints in this work are not adequate to address these degeneracies, and so Type 2 template(s) are not included in the SED models.

As discussed in Chung et al. (2014), anomalous data points within large data sets can strongly bias fits. To test for this effect, we systematically remove each photometric band from our fittings, finding that no one data point is driving our fits. However, we do find that to approach a median $\chi^2_\nu \sim 1$, we need to systematically relax the errors by ~10% of the measured fluxes. This suggests that the quoted photometric uncertainties are systematically too constraining to allow a good fit given the parameter space our templates cover. Relaxing the errors during fitting does not change our results; however, it is reflected in the reported χ^2_ν of the fits.

The inclusion of an AGN template during SED fitting is preferred if the AGN template significantly improves the fit while ruling out the null hypothesis that this improvement is by random chance. This is evaluated via the Fisher test through the F-ratio, which compares the reduced χ^2 values and degrees of freedom of the galaxy-only versus galaxy+AGN fits. The interpretation of the F-ratio and its associated probability ($F_{\rm prob}$) is subject to the Gaussian nature of the fit residuals, as well as the rarity of the relevant population, which can lead to false positives. To account for the latter effect, we calculate a corrected $F_{\rm prob}$ for all sources assuming a conservative 20% for the AGN fraction following the prescription in Chung et al. (2014). As this correction is a function of the number of degrees of freedom in the fit, it is minimal for most of our sources, which have ~17 photometric bands. A threshold of (corrected) $F_{\rm prob} \geqslant 0.93$ is adopted to accept an AGN component in the fit.

Appendix B
FSPS Spectra

To provide a representative base set of SFG models for the SED fitting of radio sources (Section 4.3.2), we generate 16 templates using the Flexible Stellar Population Synthesis stellar population code (FSPS v3.0; Conroy et al. 2009; Conroy & Gunn 2010). These templates have solar metallicity with an exponentially declining SFH (`sfh = 2`) based on a 2 Gyr old burst and e-folding time of 1 Gyr. Dust content is treated self-consistently across the spectrum. Dust attenuation is modeled according to Calzetti et al. (2000) with variable attenuation ($A_v = 0$–3 in steps of 0.2). Dust emission, dominated by PAH emission in the relevant wavelength range (0.03–30 μm), is based on the Draine & Li (2007) models. Dust emission parameters `duste_gamma = 0.02`, `duste_umin = 7`, and `duste_qpah = 2` are chosen based on the stacked posteriors of energy-balanced fits to galaxies with Herschel photometry (Leja et al. 2017); the latter is chosen to be on the lower end of the distribution found in Leja et al. (2017) in order to provide a more reasonable 3.3 μm feature, which is known to be overestimated in current modeling (B. Johnson 2020, private communication).

ORCID iDs

Stacey Alberts https://orcid.org/0000-0002-8909-8782
Wiphu Rujopakarn https://orcid.org/0000-0002-0303-499X
George H. Rieke https://orcid.org/0000-0003-2303-6519
Preshanth Jagannathan https://orcid.org/0000-0002-5825-9635
Kristina Nyland https://orcid.org/0000-0003-1991-370X

References

Akylas, A., Georgakakis, A., Georgantopoulos, I., Brightman, M., & Nandra, K. 2012, A&A, 546, A98
Akylas, A., Georgantopoulos, I., Ranalli, P., et al. 2016, A&A, 594, A73
Alberts, S., Pope, A., Brodwin, M., et al. 2016, ApJ, 825, 72
Alexander, D. M., Bauer, F. E., Chapman, S. C., et al. 2005, ApJ, 632, 736
Alonso-Herrero, A., Pérez-González, P. G., Alexander, D. M., et al. 2006, ApJ, 640, 167
Appleton, P. N., Fadda, D. T., Marleau, F. R., et al. 2004, ApJS, 154, 147
Armus, L., Charmandaris, V., Bernard-Salas, J., et al. 2007, ApJ, 656, 148
Assef, R. J., Kochanek, C. S., Brodwin, M., et al. 2008, ApJ, 676, 286
Assef, R. J., Kochanek, C. S., Brodwin, M., et al. 2010, ApJ, 713, 970
Astropy Collaboration, Robitaille, T. P., Tollerud, E. J., et al. 2013, A&A, 558, A33
Barro, G., Pérez-González, P. G., Gallego, J., et al. 2011a, ApJS, 193, 13
Barro, G., Pérez-González, P. G., Gallego, J., et al. 2011b, ApJS, 193, 30
Berta, S., Lutz, D., Santini, P., et al. 2013, A&A, 551, A100
Berta, S., Magnelli, B., Nordon, R., et al. 2011, A&A, 532, A49
Blundell, K. M., & Rawlings, S. 2001, ApJL, 562, L5
Bonzini, M., Mainieri, V., Padovani, P., et al. 2015, MNRAS, 453, 1079
Bonzini, M., Padovani, P., Mainieri, V., et al. 2013, MNRAS, 436, 3759
Brammer, G. B., van Dokkum, P. G., & Coppi, P. 2008, ApJ, 686, 1503
Brammer, G. B., van Dokkum, P. G., Franx, M., et al. 2012, ApJS, 200, 13
Brandt, W. N., & Alexander, D. M. 2015, A&ARv, 23, 1
Calzetti, D., Armus, L., Bohlin, R. C., et al. 2000, ApJ, 533, 682
Caputi, K. I., Michałowski, M. J., Krips, M., et al. 2014, ApJ, 788, 126
Ceraj, L., Smolčić, V., Delvecchio, I., et al. 2018, A&A, 620, A192
Chabrier, G. 2003, PASP, 115, 763
Chen, C.-T. J., Hickox, R. C., Alberts, S., et al. 2013, ApJ, 773, 3

Chen, C.-T. J., Hickox, R. C., Goulding, A. D., et al. 2017, ApJ, 837, 145
Chung, S. M., Kochanek, C. S., Assef, R., et al. 2014, ApJ, 790, 54
Clemens, M. S., Vega, O., Bressan, A., et al. 2008, A&A, 477, 95
Condon, J. J. 1984, ApJ, 287, 461
Condon, J. J. 1992, ARA&A, 30, 575
Condon, J. J., Anderson, M. L., & Helou, G. 1991, ApJ, 376, 95
Condon, J. J., Cotton, W. D., Fomalont, E. B., et al. 2012, ApJ, 758, 23
Condon, J. J., Kellermann, K. I., Kimball, A. E., Ivezić, Ž, & Perley, R. A. 2013, ApJ, 768, 37
Conroy, C., & Gunn, J. E. 2010, ApJ, 712, 833
Conroy, C., Gunn, J. E., & White, M. 2009, ApJ, 699, 486
Corrales, L. R., García, J., Wilms, J., & Baganoff, F. 2016, MNRAS, 458, 1345
Cutri, R. M., Rieke, G. H., & Lebofsky, M. J. 1984, ApJ, 287, 566
Dai, Y. S., Wilkes, B. J., Bergeron, J., et al. 2018, MNRAS, 478, 4238
De Rossi, M. E., Rieke, G. H., Shivaei, I., Bromm, V., & Lyu, J. 2018, ApJ, 869, 4
Del Moro, A., Alexander, D. M., Bauer, F. E., et al. 2016, MNRAS, 456, 2105
Del Moro, A., Alexander, D. M., Mullaney, J. R., et al. 2013, A&A, 549, A59
Delhaize, J., Smolčić, V., Delvecchio, I., et al. 2017, A&A, 602, A4
Delvecchio, I., Lutz, D., Berta, S., et al. 2015, MNRAS, 449, 373
Delvecchio, I., Smolčić, V., Zamorani, G., et al. 2017, A&A, 602, A3
Di Matteo, T., Springel, V., & Hernquist, L. 2005, Natur, 433, 604
Diamond-Stanic, A. M., & Rieke, G. H. 2012, ApJ, 746, 168
Dole, H., Rieke, G. H., Lagache, G., et al. 2004, ApJS, 154, 93
Donley, J. L., Koekemoer, A. M., Brusa, M., et al. 2012, ApJ, 748, 142
Donley, J. L., Rieke, G. H., Pérez-González, P. G., & Barro, G. 2008, ApJ, 687, 111
Donley, J. L., Rieke, G. H., Rigby, J. R., & Pérez-González, P. G. 2005, ApJ, 634, 169
Draine, B. T., & Li, A. 2007, ApJ, 657, 810
Durré, M., & Mould, J. 2018, ApJ, 867, 149
Eisenhardt, P. R. M., Wu, J., Tsai, C.-W., et al. 2012, ApJ, 755, 173
Elbaz, D., Dickinson, M., Hwang, H. S., et al. 2011, A&A, 533, A119
Elvis, M., Hao, H., Civano, F., et al. 2012, ApJ, 759, 6
Elvis, M., Wilkes, B. J., McDowell, J. C., et al. 1994, ApJS, 95, 1
Fanidakis, N., Baugh, C. M., Benson, A. J., et al. 2011, MNRAS, 410, 53
Farrah, D., Afonso, J., Efstathiou, A., et al. 2003, MNRAS, 343, 585
Fiore, F., Puccetti, S., Brusa, M., et al. 2009, ApJ, 693, 447
Freeman, P., Doe, S., & Siemiginowska, A. 2001, Proc. SPIE, 4477, 76
Fritz, J., Franceschini, A., & Hatziminaoglou, E. 2006, MNRAS, 366, 767
Gallimore, J. F., Axon, D. J., O'Dea, C. P., Baum, S. A., & Pedlar, A. 2006, AJ, 132, 546
Gandhi, P., Horst, H., Smette, A., et al. 2009, A&A, 502, 457
Georgantopoulos, I., & Akylas, A. 2019, A&A, 621, A28
Ghisellini, G., Haardt, F., Della Ceca, R., Volonteri, M., & Sbarrato, T. 2013, MNRAS, 432, 2818
Gim, H. B., Yun, M. S., Owen, F. N., et al. 2019, ApJ, 875, 80
González-Martín, O., Masegosa, J., García-Bernete, I., et al. 2019a, ApJ, 884, 10
González-Martín, O., Masegosa, J., García-Bernete, I., et al. 2019b, ApJ, 884, 11
Grogin, N. A., Kocevski, D. D., Faber, S. M., et al. 2011, ApJS, 197, 35
Guidetti, D., Bondi, M., Prandoni, I., et al. 2017, MNRAS, 471, 210
Hamann, F., Zakamska, N. L., Ross, N., et al. 2017, MNRAS, 464, 3431
Hao, H., Elvis, M., Civano, F., et al. 2014, MNRAS, 438, 1288
Hao, H., Elvis, M., Civano, F., & Lawrence, A. 2011, ApJ, 733, 108
Heckman, T. M., & Best, P. N. 2014, ARA&A, 52, 589
Helou, G., Soifer, B. T., & Rowan-Robinson, M. 1985, ApJL, 298, L7
Herrera Ruiz, N., Middelberg, E., Norris, R. P., & Maini, A. 2016, A&A, 589, L2
Hirschmann, M., Dolag, K., Saro, A., et al. 2014, MNRAS, 442, 2304
Hopkins, A. M., Mobasher, B., Cram, L., & Rowan-Robinson, M. 1998, MNRAS, 296, 839
Hopkins, P. F., Hernquist, L., Cox, T. J., et al. 2006, ApJS, 163, 1
Huynh, M. T., Bell, M. E., Hopkins, A. M., Norris, R. P., & Seymour, N. 2015, MNRAS, 454, 952
Ivison, R. J., Magnelli, B., Ibar, E., et al. 2010, A&A, 518, L31
Jackson, N., Tagore, A. S., Roberts, C., et al. 2015, MNRAS, 454, 287
Jagannathan, P., Bhatnagar, S., Brisken, W., & Taylor, A. R. 2018, AJ, 155, 3
Jester, S. 2005, ApJ, 625, 667
Jiang, L., Fan, X., Brandt, W. N., et al. 2010, Natur, 464, 380
Jiang, L., Fan, X., Hines, D. C., et al. 2006, AJ, 132, 2127
Juneau, S., Dickinson, M., Alexander, D. M., & Salim, S. 2011, ApJ, 736, 104
Kartaltepe, J. S., Mozena, M., Kocevski, D., et al. 2015, ApJS, 221, 11
Kellermann, K. I., Condon, J. J., Kimball, A. E., Perley, R. A., & Ivezić, Ž 2016, ApJ, 831, 168
Kellermann, K. I., Fomalont, E. B., Mainieri, V., et al. 2008, ApJS, 179, 71
Kellermann, K. I., Vermeulen, R. C., Zensus, J. A., & Cohen, M. H. 1998, AJ, 115, 1295
Kimball, A. E., & Ivezić, Ž 2008, AJ, 136, 684
Kimball, A. E., Kellermann, K. I., Condon, J. J., Ivezić, Ž, & Perley, R. A. 2011, ApJL, 739, L29
King, A. L., Miller, J. M., Raymond, J., et al. 2013, ApJ, 762, 103
Kirkpatrick, A., Alberts, S., Pope, A., et al. 2017, ApJ, 849, 111
Kirkpatrick, A., Pope, A., Charmandaris, V., et al. 2013, ApJ, 763, 123
Kirkpatrick, A., Pope, A., Sajina, A., et al. 2015, ApJ, 814, 9
Klein, U., Lisenfeld, U., & Verley, S. 2018, A&A, 611, A55
Klein, U., Wielebinski, R., & Morsi, H. W. 1988, A&A, 190, 41
Kormendy, J., & Ho, L. C. 2013, ARA&A, 51, 511
Kriek, M., van Dokkum, P. G., Labbé, I., et al. 2009, ApJ, 700, 221
Lacy, M., Storrie-Lombardi, L. J., Sajina, A., et al. 2004, ApJS, 154, 166
Lansbury, G. B., Alexander, D. M., Aird, J., et al. 2017, ApJ, 846, 20
Lansbury, G. B., Gandhi, P., Alexander, D. M., et al. 2015, ApJ, 809, 115
Lanzuisi, G., Delvecchio, I., Berta, S., et al. 2017, A&A, 602, A123
Laor, A., & Behar, E. 2008, MNRAS, 390, 847
Lehmer, B. D., Alexander, D. M., Bauer, F. E., et al. 2010, ApJ, 724, 559
Lehmer, B. D., Basu-Zych, A. R., Mineo, S., et al. 2016, ApJ, 825, 7
Leja, J., Johnson, B. D., Conroy, C., van Dokkum, P. G., & Byler, N. 2017, ApJ, 837, 170
Leroy, A. K., Evans, A. S., Momjian, E., et al. 2011, ApJL, 739, L25
Lin, H., Kirshner, R. P., Shectman, S. A., et al. 1996, ApJ, 471, 617
Lindroos, L., Knudsen, K. K., Vlemmings, W., Conway, J., & Martí-Vidal, I. 2015, MNRAS, 446, 3502
Luo, B., Brandt, W. N., Xue, Y. Q., et al. 2017, ApJS, 228, 2
Lusso, E., Comastri, A., Simmons, B. D., et al. 2012, MNRAS, 425, 623
Lyu, J., & Rieke, G. H. 2017, ApJ, 841, 76
Lyu, J., & Rieke, G. H. 2018, ApJ, 866, 92
Lyu, J., Rieke, G. H., & Alberts, S. 2016, ApJ, 816, 85
Lyu, J., Rieke, G. H., & Shi, Y. 2017, ApJ, 835, 257
Lyu, J., Rieke, G. H., & Smith, P. S. 2019, ApJ, 886, 33
Madau, P., & Dickinson, M. 2014, ARA&A, 52, 415
Magnelli, B., Elbaz, D., Chary, R. R., et al. 2009, A&A, 496, 57
Magnelli, B., Ivison, R. J., Lutz, D., et al. 2015, A&A, 573, A45
Magorrian, J., Tremaine, S., Richstone, D., et al. 1998, AJ, 115, 2285
Maini, A., Prandoni, I., Norris, R. P., Giovannini, G., & Spitler, L. R. 2016, A&A, 589, L3
Maiolino, R., & Rieke, G. H. 1995, ApJ, 454, 95
Mancuso, C., Lapi, A., Prandoni, I., et al. 2017, ApJ, 842, 95
Mao, M. Y., Huynh, M. T., Norris, R. P., et al. 2011, ApJ, 731, 79
Massardi, M., Ekers, R. D., Murphy, T., et al. 2011, MNRAS, 412, 318
McMullin, J. P., Waters, B., Schiebel, D., Young, W., & Golap, K. 2007, in ASP Conf. Ser. 376, CASA Architecture and Applications, ed. R. A. Shaw, F. Hill, & D. J. Bell (San Francisco, CA: ASP), 127
Meier, D. L. 2002, NewAR, 46, 247
Messias, H., Afonso, J., Salvato, M., Mobasher, B., & Hopkins, A. M. 2012, ApJ, 754, 120
Mignano, A., Prandoni, I., Gregorini, L., et al. 2008, A&A, 477, 459
Miller, L., Peacock, J. A., & Mead, A. R. G. 1990, MNRAS, 244, 207
Miller, N. A., Bonzini, M., Fomalont, E. B., et al. 2013, ApJS, 205, 13
Mineo, S., Gilfanov, M., Lehmer, B. D., Morrison, G. E., & Sunyaev, R. 2014, MNRAS, 437, 1698
Mohan, N., & Rafferty, D. 2015, PyBDSF: Python Blob Detection and Source Finder, ascl:1502.007
Momcheva, I. G., Brammer, G. B., van Dokkum, P. G., et al. 2016, ApJS, 225, 27
Nenkova, M., Sirocky, M. M., Nikutta, R., Ivezić, Ž, & Elitzur, M. 2008, ApJ, 685, 160
Nims, J., Quataert, E., & Faucher-Giguère, C.-A. 2015, MNRAS, 447, 3612
Owen, F. N., & Morrison, G. E. 2008, AJ, 136, 1889
Padovani, P. 2016, A&ARv, 24, 13
Padovani, P., Alexander, D. M., Assef, R. J., et al. 2017, A&ARv, 25, 2
Padovani, P., Bonzini, M., Kellermann, K. I., et al. 2015, MNRAS, 452, 1263
Peacock, J. A., & Gull, S. F. 1981, MNRAS, 196, 611
Pérez-González, P. G., Egami, E., Rex, M., et al. 2010, A&A, 518, L15
Pérez-González, P. G., Rieke, G. H., Villar, V., et al. 2008, ApJ, 675, 234
Persic, M., & Rephaeli, Y. 2007, A&A, 463, 481
Pierce, C. M., Ballantyne, D. R., & Ivison, R. J. 2011, ApJ, 742, 45
Qiu, J., Shi, Y., Wang, J., Zhang, Z.-Y., & Zhou, L. 2017, ApJ, 846, 68
Rafferty, D. A., Brandt, W. N., Alexander, D. M., et al. 2011, ApJ, 742, 3
Raginski, I., & Laor, A. 2016, MNRAS, 459, 2082
Ramos Almeida, C., & Ricci, C. 2017, NatAs, 1, 679
Ranalli, P., Comastri, A., & Setti, G. 2003, A&A, 399, 39

Ranalli, P., Comastri, A., Zamorani, G., et al. 2012, A&A, 542, A16
Rau, U., Bhatnagar, S., & Owen, F. N. 2016, AJ, 152, 124
Rawle, T. D., Altieri, B., Egami, E., et al. 2016, MNRAS, 459, 1626
Richards, E. A. 2000, PASP, 112, 1001
Richards, G. T., Lacy, M., Storrie-Lombardi, L. J., et al. 2006, ApJS, 166, 470
Rieke, G. H., Alonso-Herrero, A., Weiner, B. J., et al. 2009, ApJ, 692, 556
Rodríguez-Muñoz, L., Rodighiero, G., Mancini, C., et al. 2019, MNRAS, 485, 586
Ross, N. P., Hamann, F., Zakamska, N. L., et al. 2015, MNRAS, 453, 3932
Rujopakarn, W., Dunlop, J. S., Rieke, G. H., et al. 2016, ApJ, 833, 12
Rujopakarn, W., Nyland, K., Rieke, G. H., et al. 2018, ApJL, 854, L4
Rujopakarn, W., Rieke, G. H., Weiner, B. J., et al. 2013, ApJ, 767, 73
Rybicki, G. B., & Lightman, A. P. 1986, Radiative Processes in Astrophysics (New York: Wiley-VCH)
Santini, P., Fontana, A., Grazian, A., et al. 2009, A&A, 504, 751
Scott, A. E., & Stewart, G. C. 2014, MNRAS, 438, 2253
Seymour, N., Dwelly, T., Moss, D., et al. 2008, MNRAS, 386, 1695
Seymour, N., McHardy, I. M., & Gunn, K. F. 2004, MNRAS, 352, 131
Silverman, J. D., Mainieri, V., Salvato, M., et al. 2010, ApJS, 191, 124
Simpson, C., Martínez-Sansigre, A., Rawlings, S., et al. 2006, MNRAS, 372, 741
Skelton, R. E., Whitaker, K. E., Momcheva, I. G., et al. 2014, ApJS, 214, 24
Smolčić, V., Delvecchio, I., Zamorani, G., et al. 2017, A&A, 602, A2
Smolčić, V., Schinnerer, E., Scodeggio, M., et al. 2008, ApJS, 177, 14
Spergel, D. N., Verde, L., Peiris, H. V., et al. 2003, ApJS, 148, 175
Spinoglio, L., & Malkan, M. A. 1989, ApJ, 342, 83
Stern, D., Eisenhardt, P., Gorjian, V., et al. 2005, ApJ, 631, 163
Symeonidis, M., Georgakakis, A., Page, M. J., et al. 2014, MNRAS, 443, 3728
Tabatabaei, F. S., Schinnerer, E., Krause, M., et al. 2017, ApJ, 836, 185
Teng, S. H., Brandt, W. N., Harrison, F. A., et al. 2014, ApJ, 785, 19
Terashima, Y., & Wilson, A. S. 2003, ApJ, 583, 145
Tisanić, K., Smolčić, V., Delhaize, J., et al. 2019, A&A, 621, A139
Treister, E., Urry, C. M., & Virani, S. 2009, ApJ, 696, 110
Vattakunnel, S., Tozzi, P., Matteucci, F., et al. 2012, MNRAS, 420, 2190
Vito, F., Maiolino, R., Santini, P., et al. 2014, MNRAS, 441, 1059
Wall, J. V., & Cooke, D. J. 1975, MNRAS, 171, 9
Wall, J. V., & Peacock, J. A. 1985, MNRAS, 216, 173
White, S. V., Jarvis, M. J., Kalfountzou, E., et al. 2017, MNRAS, 468, 217
Whittam, I. H., Jarvis, M. J., Green, D. A., Heywood, I., & Riley, J. M. 2017, MNRAS, 471, 908
Williams, W. L., & Röttgering, H. J. A. 2015, MNRAS, 450, 1538
Willner, S. P., Ward, M., Longmore, A., et al. 1984, PASP, 96, 143
Willott, C. J., Rawlings, S., Blundell, K. M., Lacy, M., & Eales, S. A. 2001, MNRAS, 322, 536
Windhorst, R. A., Miley, G. K., Owen, F. N., Kron, R. G., & Koo, D. C. 1985, ApJ, 289, 494
Wu, J., Tsai, C.-W., Sayers, J., et al. 2012, ApJ, 756, 96
Xu, L., Rieke, G. H., Egami, E., et al. 2015a, ApJ, 808, 159
Xu, L., Rieke, G. H., Egami, E., et al. 2015b, ApJS, 219, 18
Xue, M., Jiang, B. W., Gao, J., et al. 2016, ApJS, 224, 23
Xue, Y. Q., Luo, B., Brandt, W. N., et al. 2011, ApJS, 195, 10
Yang, G., Chen, C. T. J., Vito, F., et al. 2017, ApJ, 842, 72
Yun, M. S., Reddy, N. A., & Condon, J. J. 2001, ApJ, 554, 803
Zajaček, M., Busch, G., Valencia-S., M., et al. 2019, A&A, 630, A83
Zakamska, N. L., & Greene, J. E. 2014, MNRAS, 442, 784
Zakamska, N. L., Lampayan, K., Petric, A., et al. 2016, MNRAS, 455, 4191